

Speleothem evidence for Late Miocene extreme Arctic amplification - an analogue for near future anthropogenic climate change?

Stuart Umbo¹, Franziska Lechleitner², Thomas Opel³, Sevasti Modestou¹, Tobias Braun^{4,5}, Anton Vaks⁶,
Gideon Henderson⁷, Pete Scott⁸, Alexander Osintzev⁹, Alexandr Kononov^{10,11}, Irina Adrian¹², Yuri
5 Dublyansky¹³, Alena Giesche^{14, 15}, Sebastian F.M. Breitenbach¹

¹Department of Geography and Environmental Sciences, Northumbria University, Newcastle-upon-Tyne, NE1 8ST, United Kingdom

²Department of Chemistry, Biochemistry and Pharmaceutical Sciences & Oeschger Centre for Climate Change Research, Bern, 2012, Switzerland

10 ³Alfred Wegener Institute Helmholtz Centre for Polar and Marine Research, Telegrafenberg A45, Potsdam, 14473, Germany

⁴Remote Sensing Centre for Earth System Research, Leipzig University, 04103, Leipzig, Germany

⁵Potsdam Institute for Climate Impact Research (PIK), Member of the Leibniz Association, 14473, Potsdam, Germany

⁶Geochemistry and Environmental Geology Division, Geological Survey of Israel, Jerusalem, 9692100, Israel

⁷Department of Earth Sciences, Oxford University, Oxford, OX1 3AN United Kingdom

15 ⁸Oceans Institute, University of Western Australia, Perth, 6009, Australia

⁹Speleoclub Arabika, Irkutsk, 664058, Russian Federation

¹⁰Irkutsk National Research Technical University, Irkutsk, 664074, Russia

¹¹Institute of the Earth's Crust, Russian Academy of Sciences, Siberian Branch, Irkutsk, 664033, Russia

¹²Lena Delta Wildlife Reserve, Tiksi, Sakha Republic, 678400 Russia

20 ¹³Institute of Geology, University of Innsbruck, Innrain 52, 6020, Innsbruck, Austria

¹⁴U.S. Geological Survey, Alaska Science Center, Anchorage, Alaska 99508, USA

¹⁵Department of Earth Sciences, Cambridge University, Cambridge CB2 3EQ, United Kingdom

Correspondence to: Stuart Umbo (stuart.umbo@northumbria.ac.uk)

25

30

Abstract. The Miocene provides an excellent climatic analogue for near future runaway anthropogenic warming, with atmospheric CO₂ concentrations and global average temperatures similar to those projected for the coming century under extreme emissions scenarios. However, the magnitude of Miocene Arctic warming remains unclear due to the scarcity of reliable proxy data. Here we use stable oxygen isotope and trace element analyses, alongside clumped isotope and fluid inclusion palaeothermometry of speleothems to reconstruct palaeo-environmental conditions near the Siberian Arctic coast during the Tortonian (8.68 ± 0.09 Ma). Stable oxygen isotope records suggest warmer-than-present temperatures. This is supported by temperature estimates based on clumped isotopes and fluid inclusions giving mean annual air temperatures between +6.6 and +11.1°C, compared with -12.3°C today. Trace elements records reveal a highly seasonal hydrological environment.

Our estimate of >18°C of Arctic warming supports the wider consensus of a warmer-than-present Miocene and provides a rare palaeo-analogue for future Arctic amplification under high emissions scenarios. The reconstructed increase in mean surface temperature far exceeds those projected in fully coupled global climate models, even under extreme emissions scenarios. Given that climate models have consistently underestimated the extent of recent Arctic amplification, our proxy data suggest Arctic warming may exceed current projections.

1 Introduction

The Arctic and sub-Arctic regions have warmed nearly four times faster than the global average since 1979 (Rantanen et al., 2022), and this disproportionate warming is expected to continue over the coming decades (Ma et al., 2022). Climate models have consistently underestimated the magnitude of this so-called Arctic amplification (Chylek et al., 2022; Rantanen et al., 2022) and show considerable discrepancies in its predicted magnitude (Smith et al., 2020; Taylor et al., 2022). Uncertainty in Arctic temperature projections are greater than for any other region on the planet (Taylor et al., 2022).

Improving Arctic climatic projections is imperative for informing local adaptation efforts. Warming is driving permafrost thaw and ice retreat, impacting ecosystems, infrastructure and access to food, whilst weather-related changes are increasing natural hazards (Ford et al., 2015). Localised warming could have global impacts. The Arctic is home to most of the planet's permafrost, a possible climate tipping element (McKay et al., 2022; Nitzbon et al., 2024). Permafrost is the Earth's largest terrestrial carbon pool (Strauss et al., 2024), and its future thaw will play a major role in potential climate trajectories. Furthermore, modelling studies suggest Greenland Ice Sheet mass loss, driven by Arctic warming, will be a major contributor to 21st century sea level rise, with the potential to significantly weaken the Atlantic Meridional Overturning Circulation (Hofer et al., 2020).

Detailed palaeoclimate records present an excellent opportunity to verify climate models and improve future projections. Whilst past warm intervals represent imperfect analogues for near future climate because of differences in climate forcing, these periods can provide important examples of planetary response to atmospheric warming. Recently, Steinthorsdottir and colleagues (2021b) proposed the Miocene (23.03 – 5.33 Ma) as a suitable palaeo-analogue for future anthropogenic climate change. The distribution of continental landmasses was similar to the present day (Steinthorsdottir et al., 2021b) and atmospheric $p\text{CO}_2$ concentrations close to modern levels. Reconstructions generally agree on atmospheric $p\text{CO}_2$ values between 400 and 600 ppm throughout the Miocene (Steinthorsdottir et al., 2021a). Whilst some estimates suggest this may have reached as high as 800 – 1000 ppm during the Miocene Climatic Optimum (MCO) (Rae et al., 2021), most studies suggest it was considerably lower, likely between 430 and 630 ppm (Sosdian et al., 2018; Super et al., 2018). Subsequent cooling of ca. 6°C was coincident with a ca. 125 ppm decline in atmospheric CO_2 (Super et al., 2018). By the Late Miocene (ca. 7 - 5.4 Ma), multiple reconstructions converge on atmospheric carbon dioxide concentrations between 300 and 500 ppm (Rae et al., 2021; Sosdian et al., 2018; Super et al., 2018), close to modern day levels (ca.420 ppm), with the upper estimate similar to those projected for the coming decades at current emission rates (Masson-Delmotte et al., 2021).

Burls et al. (2021) synthesised available proxy temperature reconstructions to deduce a global mean surface temperature of $21.21 \pm 0.56^\circ\text{C}$ for the Early Miocene. Temperatures declined rapidly following the MCO, particularly in the high latitudes, where cooling up to 8°C is observed in marine records (Herbert et al., 2016). By the Late Miocene, global mean sea surface temperature (SST) was ca. 6°C higher than present day (Herbert et al., 2016), and mean terrestrial surface temperature was ca. 4.5°C above the pre-industrial (Pound et al., 2011). Proxy reconstructions suggest a much-reduced latitudinal temperature gradient which saw Arctic mean annual temperature (MAT) 11 – 19°C warmer than present during the Middle Miocene (Steinthorsdottir et al., 2021b and references therein), declining to between 5 and 6°C above pre-industrial by the Late Miocene (Pound et al., 2012). Whilst this period saw the establishment of a stable Antarctic ice sheet (Miller et al., 2020), biomarker evidence suggests that ice free summers in the Arctic persisted (Stein et al., 2016).

Modelling reconstructions, driven by inferred Miocene atmospheric CO_2 concentrations, have consistently failed to reconstruct the high temperatures, and reduced latitudinal temperature gradient, seen in the Miocene proxy records (Goldner et al., 2014). It is unclear whether this discrepancy arises due to missing climatic feedbacks within climate models or consistent under/over estimation of atmospheric CO_2 concentrations and temperatures in proxy reconstructions, but resolving it is of importance for estimation of future warming. Here we present a multi-proxy analysis of four speleothems (cave carbonate deposits) from the Siberian Arctic to infer environmental conditions during the Tortonian Stage of the Late Miocene Subepoch. We use isotope measurements of speleothem fluid inclusions and clumped isotope analyses to estimate multi-annual mean surface air palaeotemperatures, and stable oxygen isotope and trace element data to reconstruct palaeo-hydrology and seasonality, providing a new, high precision dataset to understand Miocene climate sensitivity.

2 Study site and sample material

2.1 Study site

Samples were collected from the Taba Ba'astakh cliffs (N72.27°, E126.94°), which rise ca. 140 m above the eastern riverbank near the entrance of the Lena River delta, ca. 100 km northwest of Tiksi, Sakha Republic, Russian Federation (Fig. 1). The cliffs are composed of Carboniferous-aged carbonates (Mikhaltsov et al., 2018). Lower strata (up to ca. 50 m above current river level) comprise fine quartzitic sandstone, siltstone, sandy dolomite, and dolomitic limestone with sparse fossil coral and ostracod and foraminifera assemblages broadly linked to the Tournaisian (358.9–346.7 Ma) (Izokh and Yazikov, 2017). Above, ca. 50 m from the riverbank, bioclastic carbonate, calcareous siliciclastics and carbonates form a subsiding platform. Continuous permafrost, 400–600 m thick, is found in this region, with an active-layer thaw depth between 0.6 and 0.4 m (Boike et al., 2019). All caves encountered during the expedition contained significant ice deposits, rendering modern speleothem formation impossible. Modern tundra vegetation is sparse, consisting mostly of grasses, mosses, and lichens, with a small number of bushes (mainly polar willow). Trees are not found above the caves today.

110

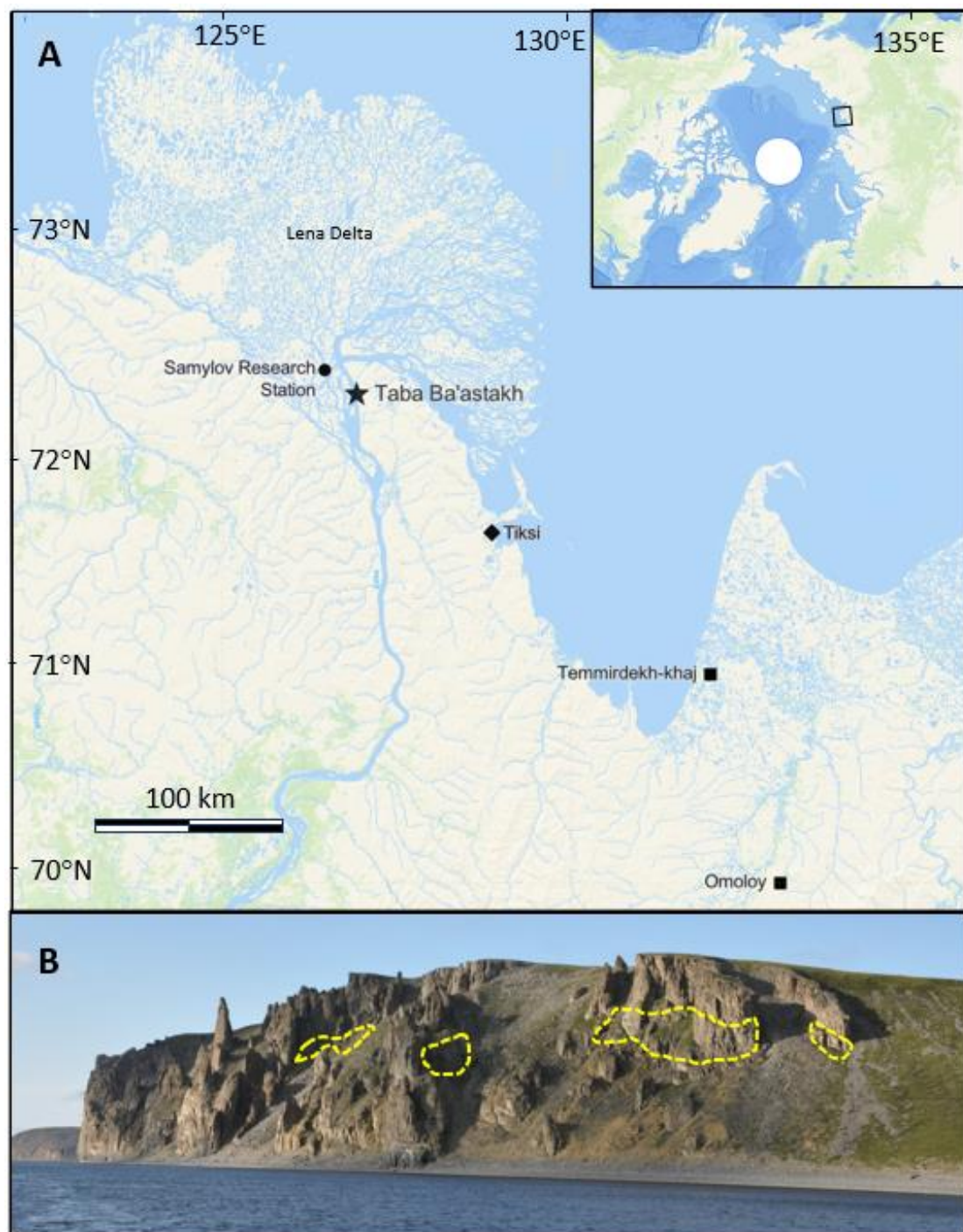


Figure 1: (A) Location of Taba Ba'astakh sampling site, Samoylov Research Station, and relevant Miocene palaeoclimate reconstruction sites: Temmirdekh-khaj and Omoloy (Popova et al., 2012). The green shading shows forested areas (Map created in Esri ArcGIS), (B) Photograph of the Taba Ba'astakh cliffs (height ca. 120 – 140 m) with cave locations outlined with yellow dashed lines (adapted from Vaks et al., accepted).

Meteorological data recorded at the Samoylov Island Research Station in the central Lena River Delta (N72.37°, E126.48°), ca. 20 km northwest of our study area, indicate a polar tundra climate (ET according to the Köppen-Geiger classification, Peel et al., (2007)), with a mean annual air temperature (MAAT) of -12.3°C, July average of +9.5°C, and February average of -32.7°C (all temperature data averaged between 1998 and 2017) (Boike et al., 2019). The closest available mean annual rainfall estimate is 309 mm (1980 - 2018), measured at the Tiksi meteorological station 90 km southeast of Taba Ba'astakh (Buchwal et al., 2023).

2.2 Sample description

Fourteen speleothem samples were collected from the base of the Taba Ba'astakh cliffs, on the bank of the Lena River in 2014. The modern caves are ice filled and inaccessible after a few meters, but erosion of the cliff face has exposed the interior of relic caves, with speleothems observed along the cliff walls. Observations of ongoing weathering of cave walls suggest that these samples originated from the cliff face 70-120 m above the sampling site where some in-situ speleothems were also found. All 14 samples have been dated to the Tortonian Stage (Vaks et al., accepted) using U-Pb dating following a modified method described in Vaks et al. (2020) and Mason et al. (2022). The ^{235}U - ^{207}Pb – $^{208}\text{Pb}/^{207}\text{Pb}$ isochron age of all samples yielded an age of 8.68 ± 0.09 Ma with a mean square weighted deviation of 1.2 (Vaks et al., accepted). Overlapping uncertainties of top and bottom ages allow only the construction of relative age-depth models along the growth profile of individual samples.

Four samples, STBB I – 1, STBB II – 7, STBB 4 – 2, and STBB 4 – 3 (Fig. 2) were selected for this study, as their high precision dates and large size make them amenable for coupled reconstruction of temperature and climate conditions at their time of deposition. All samples are composed of calcite (Vaks et al., accepted).

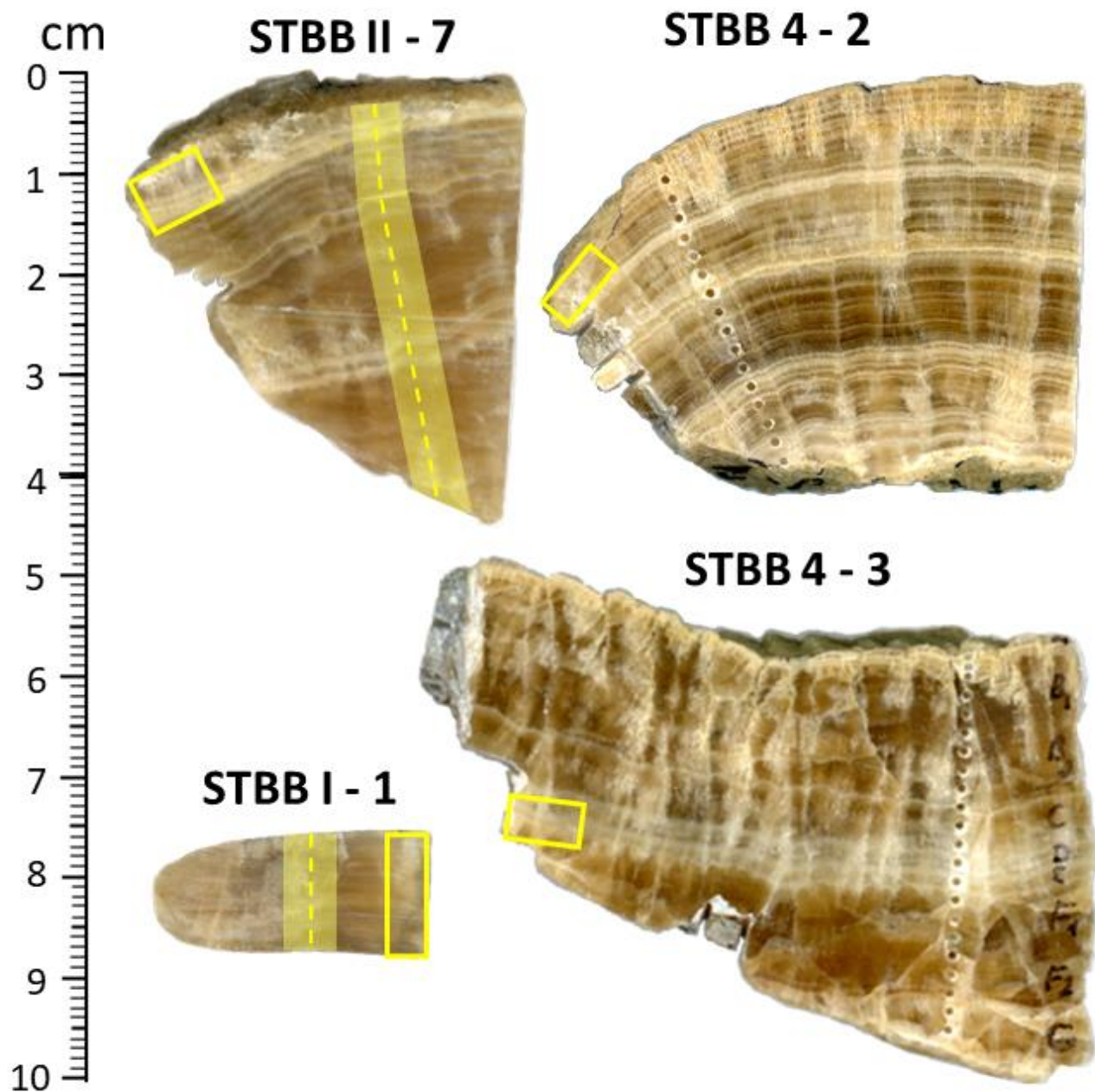


Figure 2: Speleothem samples used in this study. Thick translucent tracks, overlain with dashed lines, show the positions of stable isotope and trace element sampling profiles respectively (STBB I – 1 and STBB II – 7 only). Boxes indicate clumped isotope sampling positions.

3 Methodology

3.1 Clumped isotope geothermometry

Clumped isotope analyses for estimating speleothem formation temperatures were performed on subsamples of all four speleothems. Measurements were conducted at Northumbria University using a Nu Instruments Perspective dual inlet isotope ratio mass spectrometer coupled with an automated NuCarb preparation system. Samples were drilled from layers with well constrained ages and $325 \pm 25 \mu\text{g}$ of powder loaded into sample vials, which were then evacuated, and reacted with concentrated orthophosphoric acid at 70°C . The reactant gas was dehydrated and cleaned using standard procedures (Petersen et al., 2015). Briefly, samples were dehydrated using two liquid nitrogen cryotrap, cooled to -80°C , and scrubbed of contaminants by passing through a 1 cm static trap filled with a PorapakTM Q (Waters Corporation) absorbent material, cooled to -30°C . Each replicate digestion was measured 40 times in dual inlet mode (total measurement time ca. 40 minutes). No pressure baseline correction was required.

Final clumped isotope (Δ_{47}) values were calculated using the software Easotope (www.easotope.org; John & Bowen, 2016) and the D47 Crunch Python package (Daëron, 2021). Both methodologies used the International Union of Pure and Applied Chemistry (IUPAC) parameters for ^{17}O correction and isotopic ratios for Vienna Pee Dee Belemnite (VPDB) and Vienna Standard Mean Ocean Water (VSMOW) (Bernasconi et al., 2018; Brand et al., 2010; Daëron et al., 2016). Application of both methods allowed Δ_{47} values to be inputted into both our in-house calibration, derived using Easotope, and the composite calibration of Anderson et al. (2021), which is derived using D47 Crunch.

For the Easotope method, sample Δ_{47} values were projected onto carbon dioxide equilibrium space (I-CDES-90) following the methodology of Dennis et al. (2011), using standards ETH1, ETH2, and ETH3, and I-CDES Intercarb Δ_{47} values from Bernasconi et al. (2021). Long term instrument performance was monitored with an internal standard, Pol-2 (a natural cave pool rim deposit), giving a long-term Δ_{47} external standard deviation of 0.032 ‰ ($\Delta_{47} = 0.656 \pm 0.003 \text{ ‰}$ I-CDES-90, $T_{\Delta_{47}} = 2.4 \pm 1.0^\circ\text{C}$, $N = 65$).

Replicates were measured across multiple runs over a long period of time, similar to the sliding window approach employed by, e.g., Meinicke et al. (2020) and described by Daëron & Gray (2023). Stable isotope and Δ_{47} outliers ($> \bar{x} \pm 2\sigma$), alongside samples with elevated Δ_{48} , indicative of contamination (Eiler and Schauble, 2004), were discarded from final Δ_{47} calculations (Table S4). After pruning, a minimum of 14 replicate analyses were made for each sample such that Δ_{47} 95 % confidence intervals of $\leq 0.015 \text{ ‰}$ were achieved (i.e., $\leq 0.007 \text{ ‰}$ standard error). All Δ_{47} uncertainties are quoted as standard errors and 95% confidence intervals, according to best practices outlined by Fernandez et al. (2017).

For the D47 Crunch method, contaminated samples were pruned (identified by elevated Δ_{48} and Δ_{49}), alongside outlier ETH3 replicates ($> \bar{x} \pm 2\sigma$ for $\delta_{45} - \delta_{47}$) from each run. A linear drift correction was calculated for $\delta_{45} - \delta_{47}$ using ETH3 which was then applied to all sample and standard data. Outlier ETH1, ETH2, and ETH3 ($> \bar{x} \pm 2\sigma$ for $\delta_{45} - \delta_{47}$) were then pruned from each run before input into D47 Crunch to calculate I-CDES-90 Δ_{47} values. Stable isotope and Δ_{47} outliers ($> \bar{x} \pm 2\sigma$) were pruned from the replicate data before final Δ_{47} calculations.

Clumped isotope temperatures ($T_{\Delta 47}$) were calculated by inputting D47 Crunch derived Δ_{47} values into the composite regression of Anderson et al. (2021) and Easotope derived Δ_{47} values into an internal laboratory calibration calculated from 17 natural inorganic calcite samples precipitated at known temperatures (Fig. S1, Tables S1 and S2). The derived regression equation, calculated using the York least squares method (York et al., 2004) in the R geostats package, is:

$$\Delta_{47} = 0.0372 (\pm 0.0008) \cdot \frac{10^6}{T^2} + 0.166 (\pm 0.01) \quad (1)$$

Bracketed numbers denote one standard error. This in-house regression has a slightly lower gradient and higher intercept than the composite regression derived by Anderson et al. (2021) (gradient = 0.0391 ± 0.0004 , intercept = 0.154 ± 0.004). Measurement and calibration uncertainties were propagated together to calculate temperature uncertainty following the methods of Huntington et al. (2009).

3.2 Fluid inclusion analysis for temperature estimation

Fluid inclusion analyses were conducted on STBB I – 1 and STBB II – 7, where microscopic inspection confirmed the presence of fluid inclusions. Measurements were performed at the University of Innsbruck, Austria following the method of Dublyansky and Spötl, (2009). An aliquot of 1.5 g of carbonate was crushed in a heated crusher under He flow. The released fluid inclusion water was cryo-trapped and then admitted into the TC/EA analyser (Thermo Scientific). After pyrolysis on contact with glassy carbon at 1400°C, the evolved H_2 and CO were separated in the GC column and admitted to a Delta V Advantage mass spectrometer (Thermo Scientific). Calibration was performed by measuring various amounts of reference waters with isotopic compositions bracketing the expected compositions of the sample. Fluid inclusion isotope data are reported with respect to VSMOW. Accuracy of the measurement is 1.5 ‰ for δ^2H and 0.2 ‰ for $\delta^{18}O$.

Temperatures from fluid inclusions were calculated using the calibrations of Tremaine et al. (2011) and Coplen (2007) for water-calcite oxygen isotope fractionation.

3.3 Stable oxygen isotopes

Samples STBB I – 1 and STBB II – 7 were micromilled at 50 μm resolution along their growth length using a Sherline micromill, following the methodology outlined in Lechleitner et al. (2020), producing a total of 225 and 823 subsamples, respectively.

Stable isotope analysis was conducted at Northumbria University using a method adapted from Spötl & Vennemann, (2003). 110±10 µg of the sample was loaded into a 12 ml borosilicate exetainer tube, flushed with helium and reacted with concentrated orthophosphoric acid at 70°C. Liberated CO₂ was dried using a Gasbench II and analysed for carbon and oxygen isotope ratios.

205 All samples were measured on a ThermoScientific Delta V Isotope Ratio Mass Spectrometer coupled with a ConFlo IV. We used an in-house laboratory carbonate standard (Plessen), alongside international standards NBS18 and IAEA603, measured every 10 samples to evaluate the runs. An in-house carbonate standard (Pol-2) was used to evaluate long-term external standard deviation, achieving <0.1 ‰ for δ¹⁸O. All carbonate derived stable isotope data are reported on the VPDB scale.

3.4 Trace element analysis

210 Trace element to calcium (X/Ca) ratios of 24 trace elements (tables S7 and S8) were measured along the stable isotope sampling profiles of STBB I – 1 and STBB II – 7 at 2.6 µm resolution, using laser ablation inductively coupled plasma mass spectrometry (LA-ICP-MS) at the University of Western Australia following the methods outlined in Finestone et al. (2022).

We prioritised elements regularly utilised as hydrological proxies including Mg, Sr, and Ba (Stoll et al., 2012; Treble et al., 2015), alongside a vegetation proxy (P), indicators for detrital input (Al, Th) and heavy metals (Fe, Mn) associated with organic matter binding (Hartland et al., 2012). See supplementary tables S7 and S8 for a full list of elements analysed. The stable isotope record was aligned to the trace element record using multiple visual markers such as prominent growth layers and surface blemishes.

220 Principal component analysis (PCA) was utilised to identify common variability in the Taba Ba’astakh trace element records (Orland et al., 2014). A Gaussian kernel smoothing was applied to trace element records to remove missing data and minimise noise artefacts, before log transformation and z-score normalisation to account for the PCA’s sensitivity to variable scaling. The PCA analysis was performed using the FactoMineR package in R. We applied spectral analysis to smoothed trace element and isotope records to reveal periodicities and dominant frequencies along the speleothem growth length.

225 4 Results

4.1 Clumped isotope temperature estimates

Clumped isotope results are summarised in Table 1. The Δ₄₇ values of our samples range from 0.626 to 0.641 for the Easotope method and 0.640 to 0.656 for the D47 Crunch method, returning clumped isotope temperature (T_{Δ47}) estimates between 6.6 and 11.1°C, using our in-house calibration (T_{Δ47 Easotope}) and 5.9 and 10.5°C for the D47 Crunch method and Anderson et al. (2021) regression (T_{Δ47 Crunch}). Uncertainty in Δ₄₇ is larger using the D47 Crunch method (standard error between 0.11 and 0.14‰, 95% confidence limits between 0.022 and 0.026 ‰) than the Easotope method (standard error between 0.06 and 0.07‰, 95% confidence limits between 0.012 and 0.015 ‰). This is expected given that D47 Crunch additionally propagates

of the uncertainty associated with the normalisation standards (Daëron, 2021). This uncertainty is not accounted for using Easotope. Both Easotope and D47 Crunch produce temperatures within uncertainty of each other, with higher $T_{\Delta 47}$ uncertainty in the D47 Crunch method due to larger $\Delta 47$ standard errors and the differing methods used to propagate calibration uncertainties (section 3.1).

4.2 Fluid inclusion temperature estimate

Sample STBB I – 1 yielded 0.11 μL of fossil water with a $\delta^{18}\text{O}$ value of -17.5‰ VSMOW and a δD value of -127.7‰ VSMOW, giving a deuterium excess value (d-excess) of 12.3‰ . This value lies within uncertainty of the modern Global Meteoric Water Line (GMWL) (Craig, 1961), and ca. $+9\text{‰}$ in $\delta^2\text{H}$ above the modern Local Meteoric Water Line (LMWL) from the Samoylov Island Research Station (Spors, 2018) (Fig. S2). Since large sample volumes are required for fluid inclusion measurements, our $\delta^{18}\text{O}$ value is obtained from a speleothem section incorporating the entire growth length, representing an average of the entire speleothem. Thus, we applied a constant $\delta^{18}\text{O}$ value of -17.5‰ (VSMOW) for dripwater ($\delta^{18}\text{O}_{\text{dw}}$) across the entire calcite $\delta^{18}\text{O}$ record to obtain minimum and maximum temperature estimates. Sample STBB II – 7 failed to yield sufficient inclusion water for analysis and thus no temperature estimate could be derived from this sample. The lower end of the STBB I – 1 fluid inclusion derived temperature estimate ($T_{\text{FI}} = 9.0 - 19.2^\circ\text{C}$) overlaps with the independently derived $T_{\Delta 47}$ estimate ($T_{\Delta 47} = 11.1$).

250

255

Table 1: Clumped isotope data and temperature estimates from Taba Ba’astakh samples. N = number of replicate Δ_{47} measurements included in final Δ_{47} calculations, with the number of excluded samples in parentheses. The number of sample replicates varies between methods due to different outlier exclusion methodologies and the exclusion of replicates with insufficient standard bracketing from the Easotope method calculations. All Δ_{47} values are reported on I-CDES90. The fluid inclusion temperature (T_{FI}) from STBB I – 1 temperature range is presented for comparison with the mean in parentheses. Replicate measurement data is presented in Table S3.

Easotope method							D47 Crunch method						Fluid inclusions	
Sample	N	Δ_{47} (‰)	Δ_{47} SE (‰)	Δ_{47} 95% CI (‰)	T_{A47} (°C)	$\pm T_{A47}$ (°C)	N	Δ_{47} (‰)	Δ_{47} SE (‰)	Δ_{47} 95% CI (‰)	T_{A47} (°C)	$\pm T_{A47}$ (°C)	T_{FI} (°C) Tremaine	T_{FI} (°C) Coplen
STBB I – 1	21 (5)	0.626	0.007	0.015	11.1	2.1	25 (2)	0.643	0.011	0.022	9.6	3.2	9.0 – 19.2 (mean = 11.8)	10.9 – 21.5 (mean = 14.5)
STBB II – 7	18 (2)	0.641	0.006	0.012	6.6	1.8	14 (3)	0.640	0.013	0.025	10.5	3.8	NA	N/A
STBB 4 – 2	14 (3)	0.640	0.007	0.014	7.0	2.0	20 (1)	0.656	0.013	0.025	5.9	3.6	NA	N/A
STBB 4 – 3	14 (2)	0.634	0.007	0.014	8.7	2.4	16 (1)	0.647	0.014	0.026	8.5	4.0	NA	N/A

260

265

4.3 Stable oxygen isotopes

270 Speleothem $\delta^{18}\text{O}$ ranges between -17.5 and -14.6 ‰ VPDB, with mean values of -15.6 ‰ and -16.9 ‰ for STBB II – 7 and
STBB I – 1, respectively (Fig. 3). STBB I – 1 $\delta^{18}\text{O}$ exhibits an initial decline, reaching a minimum around 4mm where the
trend reverses. A sharp increase is observed around 7 mm where the record peaks and remains relatively constant thereafter.
The STBB II – 7 $\delta^{18}\text{O}$ record exhibits a similar initial decline of ca. 1 ‰ until ca. 20 mm, where this trend reverses. At ca. 37
mm $\delta^{18}\text{O}$ declines by ca. 1 ‰ in the final ca. 4 mm of the record.

275

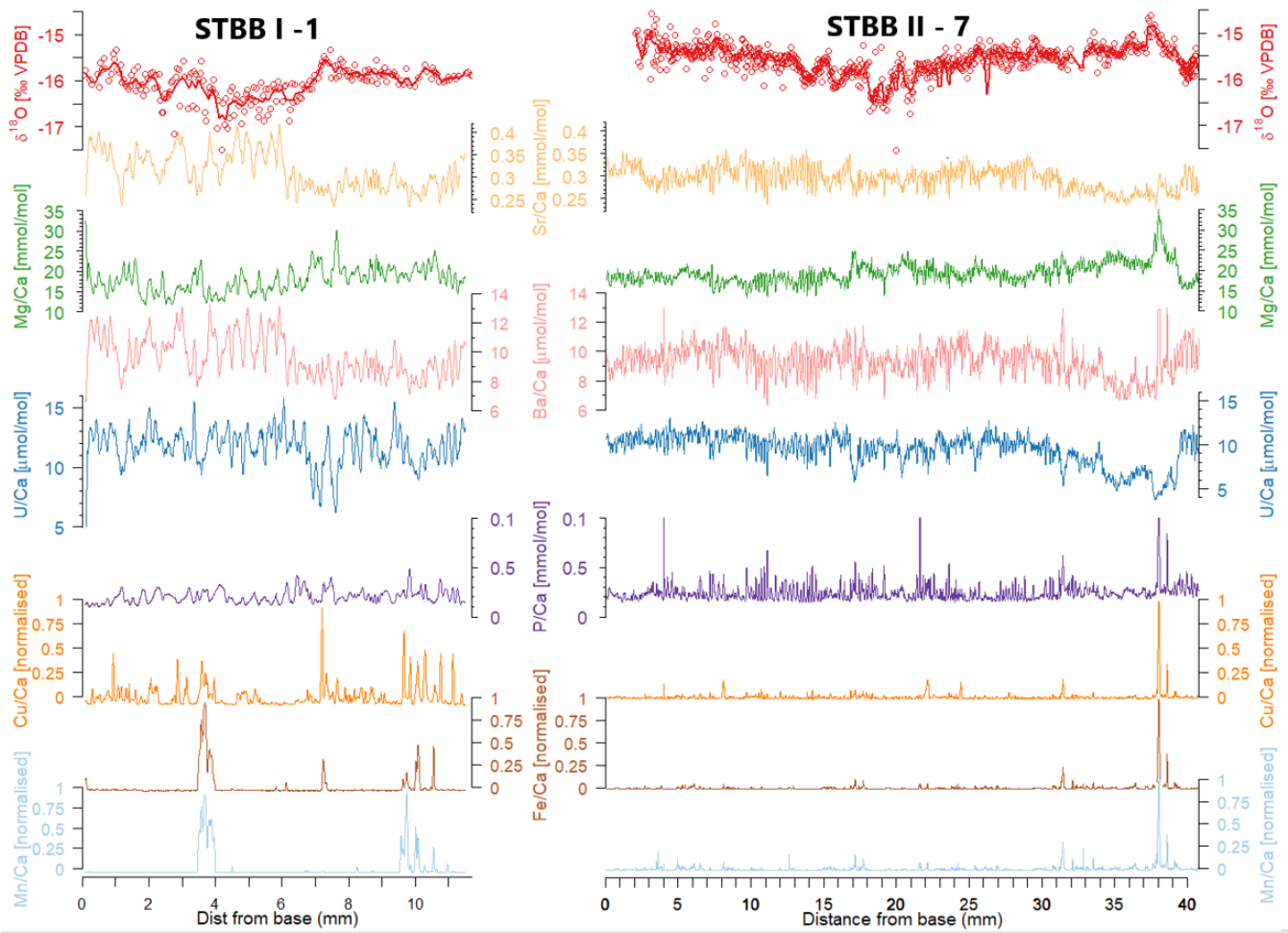


Figure 3: $\delta^{18}\text{O}$ and selected trace element records for STBB I – 1 and STBB II – 7. $\delta^{18}\text{O}$ data are shown with a 0.25 mm rolling window smoothing (thick lines). Trace elements are smoothed to 0.01 mm rolling window. Cu/Ca, Fe/Ca, and Mn/Ca ratios have been mean normalised for easier comparison between the two samples.

280 **4.4 Trace elements**

Our analysis focuses on 18 elements, predominantly cation substitutes Ba, Mg, Sr, U, and metals Cu, Co, Fe, and Mn. Concentrations of Y, La, Ce, Nd, Yb, and Th were below the detection limit and thus these elements were removed from subsequent analysis.

285 We identify two dominant principal components (PCs) in each sample, accounting for 55.5 and 70.2 % of the variance in STBB I – 1 and STBB II – 7 respectively (Table 2, Fig. S4). The first PC correlates with Ba, Sr, Mg, and U and accounts for 37 % of the variance in STBB I – 1 and 15.8 % in STBB II – 7. These elements are commonly utilised as hydrological proxies in speleothems (Tooth and Fairchild, 2003; Treble et al., 2015) and we therefore refer to this PC as the hydrological PC. This PC also correlates with Na, P, and S in STBB I – 1. The second PC correlates with B, Fe, Mn, and Pb in both samples (Al, Cu, 290 Co, Li, P, and Rb are also included in STBB II – 7) and accounts for 18.5 % of the variance in STBB I – 1 and 54.4 % in STBB II – 7. These elements are commonly associated with detrital input via flushing (Hartland et al., 2012) and we therefore refer to this PC as the detrital PC herein.

Spectral analysis revealed strong cyclicity in the hydrological PC elemental ratios (Ba, Mg, Sr, and U) in both samples, with 295 dominant wavelengths at ~ 0.3 mm and 0.5 mm in STBB I – 1, and 0.2 mm in the STBB II – 7 (Fig. S3). We also observe cyclicity in P (~ 0.3 mm and 0.5 mm in STBB I – 1, ~ 0.2 – 0.25 mm in STBB II – 7) and Cu (~0.2 mm, in STBB I – 1 only). Detrital PC metals remain relatively constant with sporadic spikes (Fig. 3).

300 **Table 2: Results of multivariate principal component analysis on Taba Ba’astakh speleothem samples. Two major elemental groupings are highlighted: The hydrological principal component, defined by elements Ba, Mg, P, Sr, U and the detrital principal component defined by elements Al, B, Cu, Co, Fe, Mn, Rb, Pb.**

STBB I – 1			STBB II – 7		
	% of variance explained	Elements		% of variance explained	Elements
Hydrological principal component	37	Ba, Cu, Mg, Na, P, S, Sr, U	Hydrological principal component	15.8	Ba, Mg, Sr, U
Detrital principal component	18.5	B, Fe, Mn, Pb	Detrital principal component	54.4	Al, B, Cu, Co, Fe, Li, Mn, P, Rb

5 Discussion

The Late Miocene climate is widely accepted to have been several degrees warmer than today. Global SSTs were ca. 6°C warmer than present (Herbert et al., 2016) and mean global surface temperature was ca. 4.5°C above pre-industrial (1870- 305 1900) (Pound et al., 2011). Most temperature estimates for the Miocene stem from marine sediments, and terrestrial data from

high northern latitudes are exceedingly sparse (e.g., Popova et al., 2012). Our speleothem records give a rare insight into terrestrial high latitude environmental changes, including temperature and hydrological conditions during this period.

310 Taba Ba'astakh lies deep within the modern continuous permafrost zone with a MAAT of -12.3°C . We infer a mean annual ground temperature (MAGT) of -8.4°C , which we calculate by averaging temperature along a 27 m borehole at the Samoylov Island Research Station (Boike et al., 2013). Since speleothem growth depends on liquid water supply, their presence at Taba Ba'astakh indicates a much warmer climate at the time of their formation (8.68 ± 0.09 Ma).

5.1 Quantitative Tortonian temperature estimates

For comparison we calculated our clumped isotope temperatures using both the Easotope software and our in-house calibration, 315 and the D47 Crunch data reduction algorithm with the composite calibration of Anderson et al. (2021). Both methods produce temperatures within uncertainty, giving confidence in our reconstructions. $T_{\Delta 47}$ uncertainty is greater for the D47 Crunch method due to propagation of the uncertainty in normalisation standards and the different method used to calculate calibration uncertainty (section 3.1). We also provide a direct comparison between clumped isotope and fluid inclusion-based temperature estimates on one sample (STBB I – 1), with the $T_{\Delta 47}$ estimates ($T_{\Delta 47 \text{ Easotope}} = 9.6 \pm 6.0^{\circ}\text{C}$ and $T_{\Delta 47 \text{ Crunch}} = 11.1 \pm 2.1^{\circ}\text{C}$) 320 overlapping with the T_{FI} estimates of both Tremaine et al. (2013) ($9.0 - 19.2^{\circ}\text{C}$, mean = 11.8°C) (Table 1) and Coplen et al. (2007) ($10.9 - 21.5^{\circ}\text{C}$, mean = 14.5°C) calibrations (Table 1). A full discussion of temperature reconstruction uncertainties is given in the SOM. Herein we limit our discussion to temperatures derived using the Easotope method and our in-house calibration since it is derived solely from subaqueous cave carbonates precipitated at temperatures similar to our samples. Both methods give similar mean temperatures across all four samples (mean $T_{\Delta 47 \text{ Easotope}} = +8.4^{\circ}\text{C}$ compared. with mean $T_{\Delta 47 \text{ Crunch}}$ 325 $= +8.6^{\circ}\text{C}$).

The large sample sizes required for clumped isotope analysis (ca. 4 mg) make sampling of individual growth layers impossible and thus our temperature estimates derive multi-annual means. The long-held assumption that cave temperature corresponds to mean surface temperature (e.g. Wigley & Brown, 1976) has been questioned (e.g. Domínguez-Villar et al., 2013). Cave 330 temperature is impacted by numerous factors including ventilation (Pflitsch and Piasecki, 2003), thermal conductivity rates through the overburden (Domínguez-Villar et al., 2013), and vegetation and snow cover (Domínguez-Villar et al., 2013; Töchterle et al., 2024) which can all act to produce offsets of several degrees between the surface and the cave environment.

Since erosion has mostly removed the Miocene overburden and brought our samples to the surface, it is impossible to know 335 the full impact that ventilation and conduction of heat may have had on the Taba Ba'astakh cave temperatures. We suggest the insulating effects of winter snow and shading from summer vegetation likely counteracted each other with minimal overall effect. For instance, in cold regions, snow acts to insulate the ground, reducing heat loss to the atmosphere (Molnar, 2022). This insulating effect has been shown to lead to cave temperatures $5-7^{\circ}\text{C}$ higher than surface air temperatures in cold regions

with persistent (ca. 233 days per year) snow cover (Töchterle et al., 2024). Our $T_{\Delta 47}$ reconstructions between 6.6 and 11.1°C suggest a mean annual surface temperature between modern day Stockholm (Moberg, 2021) and London (Met Office, 2024), which experience significantly less than 233 days of snow cover per year. We therefore envisage limited effect of snow insulation at Taba Ba'astakh. In addition, there is palynological evidence that the Miocene treeline stretched as far north as 80°N (Steinthorsdottir et al., 2021b) and thus it is reasonable to assume a degree of forest cover at Taba Ba'astakh during that time. Monitoring studies in Eagle Cave; Spain, showed that transition from shrubland to forest resulted in a reduction in cave temperature up to 2°C due to changes in insolation and modification of soil properties (Domínguez-Villar et al., 2013). Given the higher latitude of Taba Ba'astakh it would be reasonable to assume a reduced impact from insolation shielding compared with Eagle Cave however, a small offset ($\pm 2^\circ\text{C}$) is possible between our cave reconstructions and surface temperatures. Given global average sea levels ca. 10 m higher during the Late Miocene compared with modern (Miller et al., 2005), Taba Ba'astakh might have occupied a more coastal position than the present day. In the modern Arctic, lingering summer sea ice can act to reduce coastal air temperatures compared with inland locations at the same elevation (e.g. Tuktoyaktuk and Inuvik in the Canadian Arctic (Hamma, 2022)) through increased albedo and latent heat effects (Vihma, 2014). Miocene Arctic Sea ice was much reduced compared to the modern day (Stein et al., 2016) suggesting this effect may be limited. Nearby cold month temperature reconstructions from the coastal site Temmirdekh-khaj (Fig. 1) of between -2.8°C and + 1.1°C (Popova et al., 2012), considerably warmer than modern, support this notion, although we cannot rule out the possibility of lingering cold season sea ice reducing temperatures more than equivalent latitude inland locations.

360

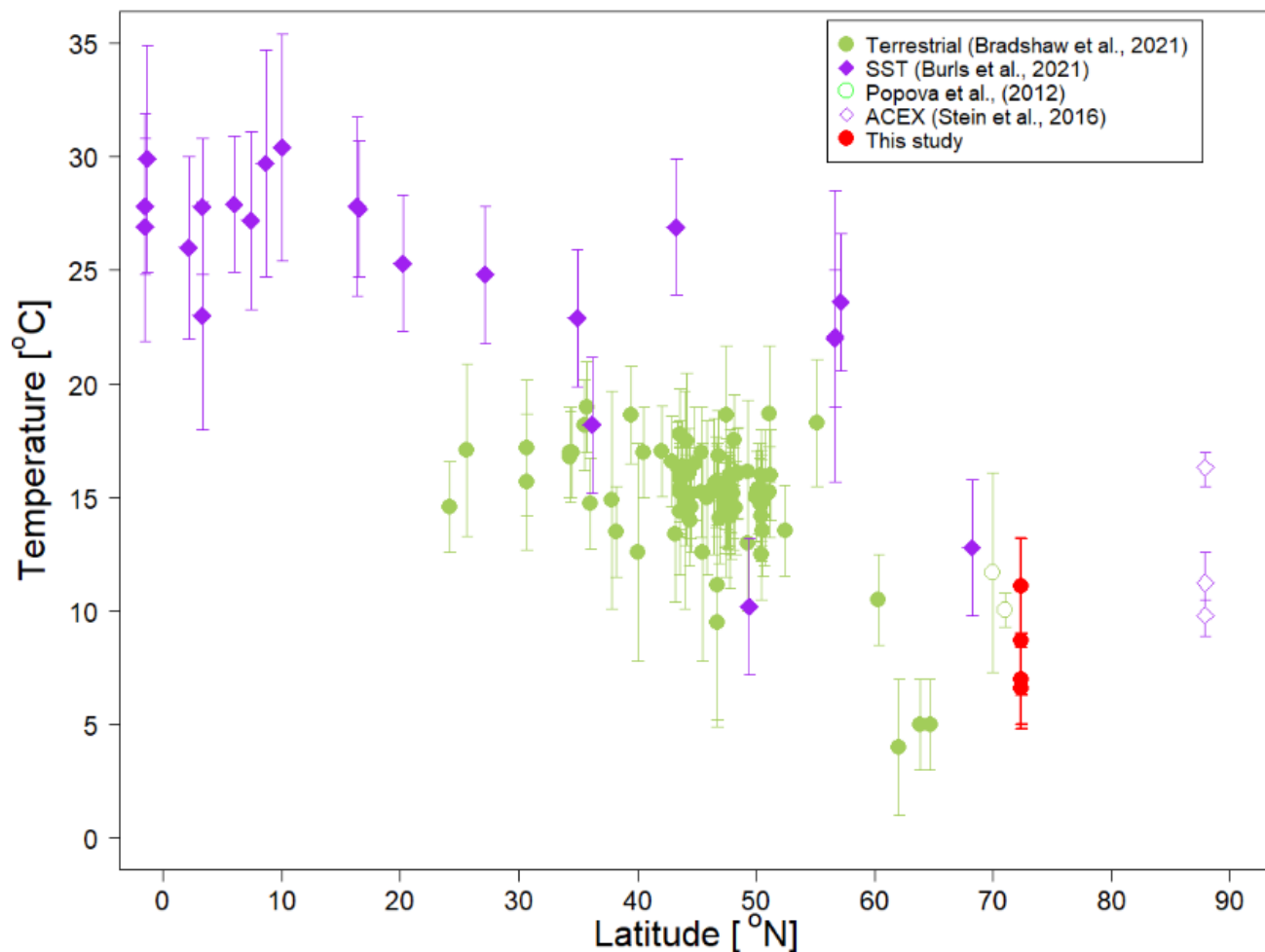


Figure 4: Compiled Northern Hemisphere Late Miocene temperature reconstructions. Green filled circles are Tortonian terrestrial mean annual temperatures reconstructions from the Bradshaw et al. (2012) database with additional sites Temmirdekh-khaj and Omoloy from Popova et al. (2012) shown unfilled. Error bars for terrestrial reconstructions show minimum and maximum estimates. The Late Miocene SST dataset from Burls et al. (2021) is shown as purple diamonds with error bars showing uncertainty in reconstruction estimate. Additional SST estimates from the ACEX borehole are shown as unfilled purple diamonds (Stein et al., 2016). ACEX borehole temperatures show the average of the four different Alkenone derived temperature calibrations quoted in Stein et al. (2016), with error bars showing the maximum, and minimum values. Both terrestrial and SST datasets have been filtered to show only data with age uncertainties overlapping our Taba Ba’astakh estimates. The red circles are the four Taba Ba’astakh clumped isotope temperature reconstructions from this study.

To our knowledge, the Taba Ba’astakh temperature reconstructions are the most northerly terrestrial Tortonian MAAT estimates to date and support the consensus of a reduced latitudinal temperature gradient during the Late Miocene (Burls et al., 2021; Gaskell et al., 2022). Our temperature estimates agree well with independent high latitude temperature reconstructions (Fig. 4). Late Miocene fossil pollen assemblages from nearby sites Temmirdekh-khaj (132°E, 71°N) and Omoloy (133°E, 70°N) (Fig. 1) yield MAAT estimates between 7.3 and 16.1°C (Popova et al., 2012). The same authors infer

a Late Miocene MAAT of 9.7°C for the whole of eastern Siberia. Exceptionally high summer SSTs between 10 and 16°C have been reconstructed for the Arctic Ocean at the Lomonosov Ridge (88.5°N) (Stein et al., 2016). Our temperature reconstructions provide new evidence of terrestrial MAAT ca. 18 to 23°C warmer than present in the Siberian Arctic during the Tortonian. This is far in excess of negative temperatures simulated by models of the Alaskan Arctic during the Middle Miocene (Goldner et al., 2014) and the ca. 3.5°C above present day zonal mean estimated in general circulation modelling of the Tortonian (Micheels et al., 2007). Thus, our findings confirm the long-established discrepancy between model simulations and proxy reconstructions with the most northerly terrestrial Miocene proxy temperature record to date and suggest that Miocene Arctic amplification is not accurately captured by general circulation models.

Since a Tortonian global mean surface temperature of 4.5°C above pre-industrial (Pound et al., 2011) was similar to the 2 – 5°C projected for the end of the century projections under high emissions scenarios (Masson-Delmotte et al., 2021), our findings provide estimates for end-of-century Arctic temperature amplification under extreme levels of anthropogenic warming. Our estimates are considerably higher than the ca. 10 - 12°C of Arctic warming by the end of the century projected in modelling studies (Nazarenko et al., 2022; Xie et al., 2022) and exceed reconstructions for the Middle-Pliocene Warm Period (3.3 - 3.0 Ma) which suggested Arctic surface air temperature warming of 7.2°C given global mean temperatures 3.2°C above pre-industrial (de Nooijer et al., 2020).

Our estimates provide useful constraints on near-future Arctic warming, but we emphasise that different planetary scale boundary conditions in the Miocene compared with today mean our deep-time reconstructions provide imperfect analogues for anthropogenic warming. Whilst the Miocene marked a large-scale expansion of global ice sheets, both northern and southern hemisphere ice sheets were highly dynamic, particularly in Greenland which was likely only partially glaciated (Steinthorsdottir et al., 2021b). Evidence from ice-wedge pseudomorphs suggests the onset of high-latitude Northern Hemisphere permafrost formation occurred in the Late Pliocene (~3 Ma) (Opel et al., 2025) and it is very likely that the Northern Hemisphere was permafrost-free during the Tortonian (Vaks et al., accepted). These, and other, slow planetary-scale feedbacks will have played a major role in the Miocene global energy budget that are unlikely to be of similar significance in driving near future temperatures.

405

5.2 Stable oxygen isotope records

410 Both Taba Ba'astakh speleothem $\delta^{18}\text{O}$ records show very negative values (means: -15.6‰ and -16.9‰). Modern studies have shown that dripwater $\delta^{18}\text{O}$ ($\delta^{18}\text{O}_{\text{dw}}$) predominantly reflects changes in $\delta^{18}\text{O}$ of precipitation ($\delta^{18}\text{O}_{\text{p}}$) above a cave (Baker et al., 2019) which, at high latitudes, is largely driven by temperature (Dansgaard, 1964). Monthly mean values of $\delta^{18}\text{O}_{\text{p}}$ from both the Samoylov Island Research Station (2013-2017) and Tiksi (2004-2017) are highly correlated to mean monthly air temperatures (Spors, 2018). Thus, we interpret $\delta^{18}\text{O}_{\text{p}}$, and in turn $\delta^{18}\text{O}_{\text{dw}}$ and speleothem $\delta^{18}\text{O}$, as indicative of temperature
415 variations at Taba Ba'astakh.

Similarly negative $\delta^{18}\text{O}$ values (ca. -16 to -11‰) are found in Greenland speleothems that formed during marine isotope stage (MIS) 15a – 14 (Moseley et al., 2021), a Middle-Pleistocene period of unusually warm and prolonged interglacials (Rodrigues et al., 2011; Hao et al., 2015). Holocene Arctic speleothem reconstructions are absent from the literature; however, the Taba
420 Ba'astakh isotope records agree well with modern Holocene values found in central Siberia 15-20 degrees latitude farther south at Botovskaya Cave (55°N), Okhotnichya Cave (52°N) (ca. -18 to -13‰) (Lechleitner et al., 2020), and Kinderlinskaya Cave (54°N) (ca. -14 to -11‰) (Baker et al., 2017). We note that the more negative $\delta^{18}\text{O}$ of the Miocene Ocean may have compounded a shift to more negative $\delta^{18}\text{O}$ values (Westerhold et al., 2020), but this would have been somewhat offset by reduced continentality at Taba Ba'astakh (generally associated with positive shifts in $\delta^{18}\text{O}$) given the ca. 10 m higher global
425 sea level (Miller et al., 2005). Given these competing influences we do not propose any firm assertions on the impact source values of $\delta^{18}\text{O}$ compared with the modern day on the $\delta^{18}\text{O}$ signal. Thus, we assume that the stable oxygen isotope records from Taba Ba'astakh support the independent temperature estimates of a much higher MAAT during the Tortonian than at present.

5.3 $\delta^{18}\text{O}$ signal of palaeo-dripwater

We estimate $\delta^{18}\text{O}_{\text{dw}}$ by using the clumped isotope derived temperatures in the temperature dependent water-calcite oxygen
430 isotopic fractionation relationship from Tremaine et al. (2011) (Table 3). Given the control of $\delta^{18}\text{O}_{\text{p}}$ on $\delta^{18}\text{O}_{\text{dw}}$, the latter provides an estimate for $\delta^{18}\text{O}_{\text{p}}$. Due to the large sample sizes required for clumped isotope analysis, the samples integrate multiple growth layers and therefore $\delta^{18}\text{O}_{\text{dw}}$ values reflect multi-annual means.

$\delta^{18}\text{O}_{\text{dw}}$ ranges between $-17.6 \pm 0.4\text{‰}$ and $-18.4 \pm 0.4\text{‰}$ (VSMOW), within error of the fluid inclusion measurement from
435 STBB I – 1 ($-17.5 \pm 1.0\text{‰}$). Agreement between these two independent $\delta^{18}\text{O}_{\text{dw}}$ derivations provides additional confidence in our estimate. We stress that this assessment does not consider the influence of additional post-precipitation evaporative processes that complicate isolation of a pure precipitation signal from speleothem fluid inclusions (Lachniet, 2009).

Assuming $\delta^{18}\text{O}_{\text{dw}}$ reflects $\delta^{18}\text{O}_{\text{p}}$, our reconstructed values for the Tortonian suggest a mean annual precipitation regime between
440 the modern summer (-15.9‰) and autumnal regimes (-19.1‰) (modern annual mean = -21.6‰) (Bonne et al., 2020) .

Table 3: Dripwater isotopic composition estimates for the four Taba Ba’astakh speleothems. $\delta^{18}\text{O}_{\text{cc}}$ is the $\delta^{18}\text{O}$ of calcium carbonate. $\delta^{18}\text{O}_{\text{cc}}$ uncertainties are standard errors. $\delta^{18}\text{O}_{\text{dw}}$ uncertainty is calculated from propagation of T_{A47} and $\delta^{18}\text{O}_{\text{cc}}$ uncertainties.

Sample	T_{A47} ($^{\circ}\text{C}$)	$\delta^{18}\text{O}_{\text{cc}}$ (‰, VPDB)	$\delta^{18}\text{O}_{\text{dw}}$ (‰, VSMOW)	$\delta^{18}\text{O}_{\text{FI}}$ (‰, VSMOW)
STBB I – 1	11.1 ± 2.1	-16.02 ± 0.01	-17.6 ± 0.4	-17.5 ± 1.0
STBB II – 7	6.6 ± 1.8	-15.86 ± 0.01	-18.3 ± 0.4	
STBB 4 – 2	7.0 ± 2.0	-16.01 ± 0.01	-18.4 ± 0.4	
STBB 4 – 3	8.7 ± 2.4	-15.87 ± 0.01	-17.9 ± 0.5	

445 **5.4 Seasonal hydrological regime**

We propose that the cyclical behaviour of trace elements is driven by a strong seasonal hydrological regime at the time of speleothem deposition. The identified hydrological PC groups in both STBB I – 1 (PC1) and STBB II – 7 (PC2) are associated with element ratios widely utilised as hydrological proxies: most commonly Mg/Ca, Sr/Ca and Ba/Ca (e.g., Tooth & Fairchild, 2003; Treble et al., 2015). These alkali metals are transported via dripwaters and substituted into the carbonate lattice during speleothem deposition. In periods of low throughflow, Ca is preferentially removed from dripwaters through prior carbonate precipitation (PCP), increasing relative concentrations of Mg, Sr, and Ba.

Correlation of Sr and Mg is often used as an indicator of PCP from infiltration waters before they reach the speleothem formation site (Wassenburg et al., 2020). Sr/Ca and Mg/Ca exhibit no consistent relationship in either Taba Ba’astakh sample, with periods of high correlation interspersed with periods of no correlation (Fig. S5). Deviation from constant Mg/Ca vs Sr/Ca ratios can arise from growth rate variability (Sliwinski et al., 2023) and changing mixing ratios of dripwater solutions derived from multiple geological endmembers (Tremaine and Froelich, 2013). Dating constraints hinder identification of growth rate variability in the Taba Ba’astakh records, however, Sr/Ca and Mg/Ca decoupling could arise from periods of hydrological rerouting or changing endmember dissolution rates between the carbonate and the overlying dolomitic limestone (Izokh and Yazikov, 2017) altering Mg/Ca concentration input.

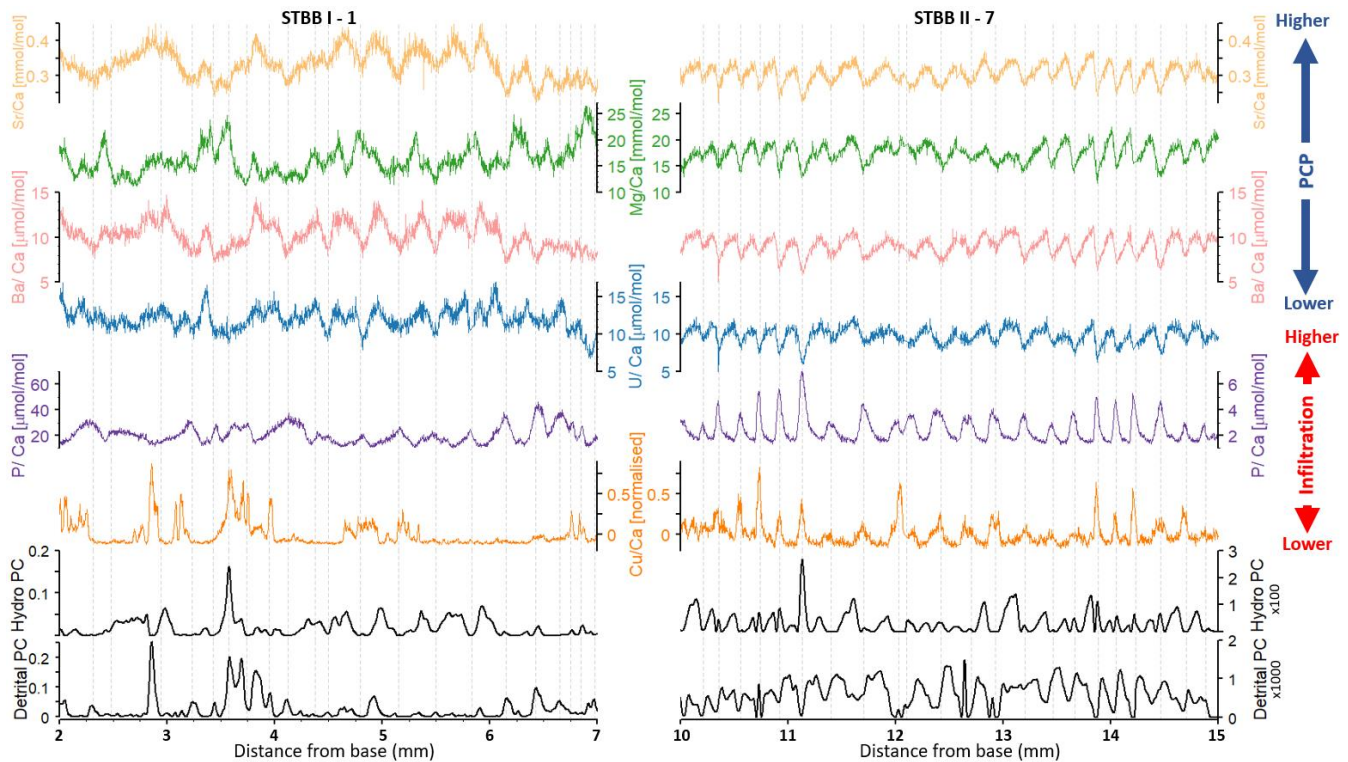


Figure 5: High resolution trace element concentrations, and major principal components along the STBB I – 1 and STBB II – 7 sampling profiles. Cu/Ca ratio has been mean-normalised for easier comparison between the two samples. Grey dashed vertical lines mark the positions of Sr/Ca troughs.

Tremaine and Froelich (2013) showed that in order to diagnose Mg/Ca and Sr/Ca as reliable ‘wet vs. dry’ proxies, Sr/Mg must remain constant along the entire sampling profile. Whilst this is not the case in the Taba Ba’astakh records, Sr/Ca is remarkably highly correlated with Ba/Ca ($r = 0.98$, $p\text{-value} < 0.01$ in STBB I – 1 and $r = 0.55$, $p\text{-value} < 0.01$ in STBB II – 7) and U/Ca ($r = 0.59$, $p\text{-value} < 0.01$ in STBB II – 7 and $r = 0.83$, $p\text{-value} < 0.01$ in STBB II – 7) along the entire growth length of both Taba Ba’astakh samples (Figs. S3 and S4). Ba/Ca has been extensively utilised as a PCP proxy (e.g. Stoll et al., 2012) and might constitute a more robust PCP proxy that is less likely affected by host rock composition at Taba Ba’astakh. Few studies have considered U/Ca as potential indicator of infiltration changes. Dripwater U is derived from bedrock dissolution and is readily incorporated into the calcite lattice (Oster et al., 2023). The strong correlation of U with both Sr and Ba in the Taba Ba’astakh records suggests that U/Ca may also reflect changes in PCP in the Taba Ba’astakh records. Finally, P/Ca is also included in the hydrological principal component in STBB I – 1, and is strongly anticorrelated with Sr, Ba, and U. P is scavenged from infiltration water during calcite precipitation, thus decreasing P/Ca in dripwater during periods of elevated PCP (Johnson et al., 2006) — as is observed in the Taba Ba’astakh records (indicated by elevated Sr/Ca, Ba/Ca and U/Ca, Fig. 5).

The detrital principal component is characterised by metals which are commonly associated with organic matter flux into the cave (Hartland et al., 2012). These metals are poorly soluble and colloiddally transported through organic matter binding during soil infiltration (Hartland et al., 2012). Hartland et al. (2012) demonstrated Cu and Co organic binding by showing speleothem Cu/Ca vs Co/Ca ratios in line with those predicted based on n1 NICA-Donnan humic and fulvic binding affinity ratios (Milne et al., 2003). We repeat this calculation for our records and find that the measured Cu/Ca vs Co/Ca ratios show good agreement with predicted ratios in STBB II – 7 (Fig. S6), confirming these metals are indeed derived from organic binding in this sample. There is poor agreement between predicted and measured ratios in STBB I – 1 suggesting detrital metals in this sample are not associated with organic binding. Phosphorus is also included in the detrital principal component in STBB II – 7. P supply has been linked with vegetative leaching during storm events (Pionke et al., 1997) with maximum P/Ca linked to elevated infiltration rates (Borsato et al., 2007). Thus, the strong positive correlation observed between P and organically bound metals provides further evidence that these element variations are reflecting infiltration rates in STBB II – 7.

We present a subsection of the trace element records in Fig. 5 where correlation between Mg and other hydrological proxies is highest to illustrate the relationship between hydrological and detrital proxies. In STBB II – 7, maxima in PCP controlled elements Sr, Mg, Ba and U coincide with minima in the infiltration-controlled elements P and Cu. Thus, wet seasons are identified as maxima in infiltration proxies (Cu/Ca and P/Ca), and minima in the PCP proxies Sr, Mg, Ba, and U. The opposite is true for dry seasons. The relationship between detrital infiltration and PCP proxies is less apparent in STBB I – 1 (Fig. 5), where we have demonstrated that detrital proxies are not controlled by organic matter influx (Fig. S6). However, strong cyclicity is observed in all PCP proxies, as well as P, which shows a similar anticorrelation with PCP proxies as in STBB II – 7.

Spectral analysis reveals dominant cycles corresponding to distances of 0.3 and 0.5 mm and 0.2 mm in STBB I – 1 and STBB II – 7 respectively (Fig. S3). Our assertion that these cycles are annual is supported by the observed alignment of the Sr/Ca record with annual banding in STBB II – 7 (Fig. S7), identified by changes in the visual greyscale. We use the free ImageJ software to extract grey values (the intensity of light carried in a single pixel) along the growth length of a high-resolution composite image STBB II – 7 thin sections (Breitenbach and Marwan, 2023). In this way, annual growth bands were identified. Sr/Ca peaks coincide with greyscale peaks (brighter layers). Thus, our trace element periods reflect growth rates of 200 μm (STBB II – 7) and 300 μm (STBB I – 1) a year, similar to those observed in modern temperate regions (Johnson et al., 2006; Sherwin and Baldini, 2011).

We compare Miocene and modern-day hydrological seasonality using a 20-year instrumental record of rainfall from the nearby Samoylov Island Research Station. We combined common hydrological proxies Sr/Ca, Ba/Ca, U/Ca, Mg/Ca, and P/Ca to obtain a single representative proxy-stack-average timeseries and aligned it to the instrumental record using dynamic time warping (Berndt & Clifford, 1994) (See SOM for details, Fig. S8). While this methodology does not eliminate the considerable

challenges of comparing palaeoseasonal proxy data to modern seasonality, it yields a pseudo-seasonal time axis that allows us to estimate precipitation seasonality in a comparable fashion for both sets of records. We compared the aligned modern and
515 Miocene hydrological seasons using a spectral seasonality measure. Precipitation seasonality is quantified by the total spectral power $|P|_s$ summed over the spectral band that closely encapsulates the seasonal peak (Fig. S9). Higher power in the seasonal band is interpreted as a more pronounced/stable seasonal signal. Detailed methodology is given in the supplementary materials.

The combined hydrological proxy records suggest a stronger seasonal precipitation regime during the Tortonian (i.e. a more
520 pronounced seasonal cycle) compared with modern day conditions (Fig. 6). This is true of both samples, with significantly higher median spectral power in the seasonal band in the Miocene compared with the modern. We recognise the limitations in the modern record which, whilst the closest available modern precipitation timeseries, measures only the liquid fraction and not snowfall, which constitutes ca. 30% total precipitation at the Samoylov Research Station (Boike et al., 2013). However, exclusion of the winter snow component within the modern record will create an apparent stronger seasonal contrast. Given
525 that our Tortonian hydrological proxy record exhibits a stronger seasonality measure than this modern rainfall record, we argue this reinforces our finding of a more seasonal hydrological regime in the Tortonian.

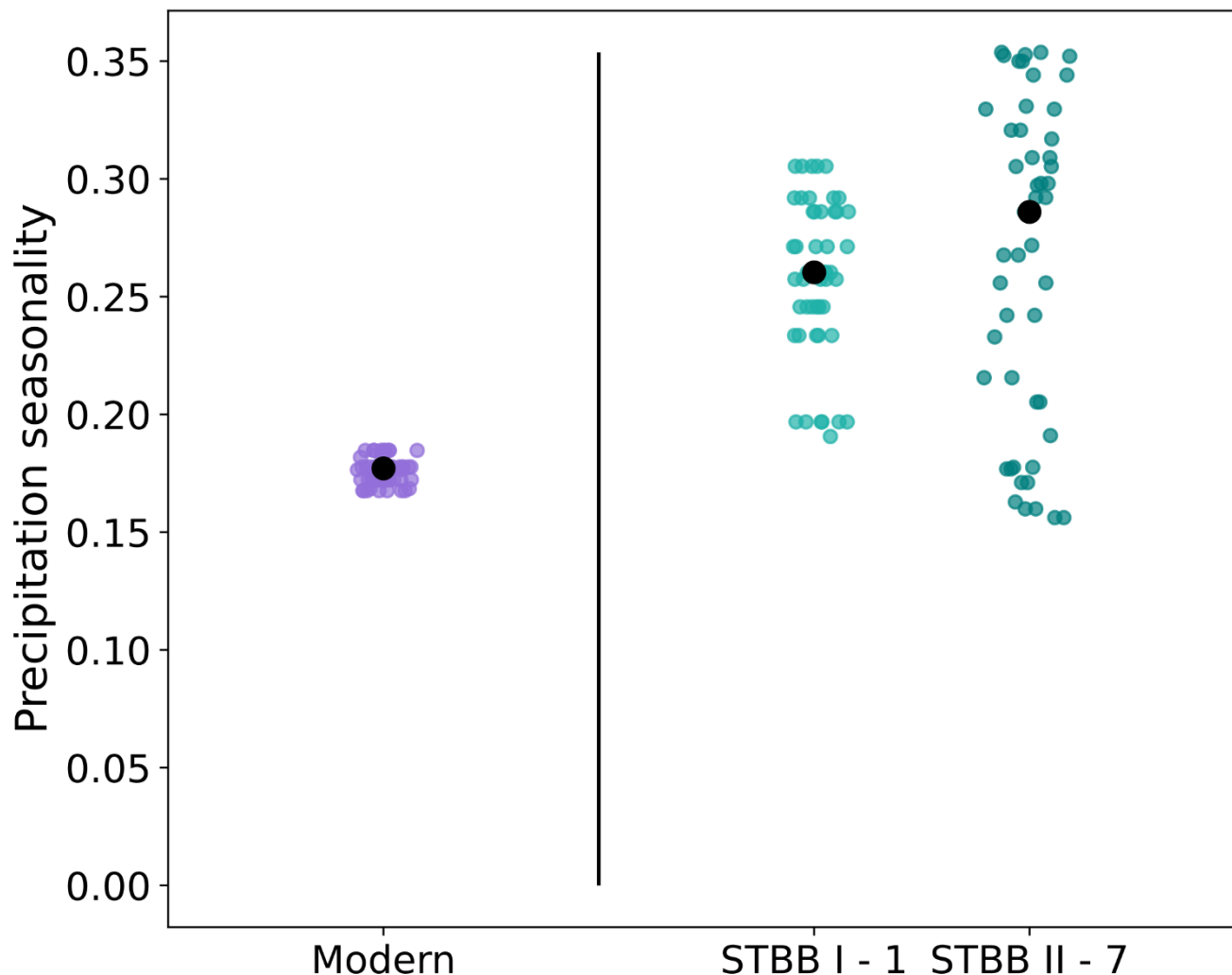


Figure 6: Reconstructed precipitation seasonality ($|P|_s$ summed over the seasonal peak spectral band) in Tortonian samples STBB I – 1 and STBB II – 7, compared with the modern day. An alignment procedure based on dynamic time warping allows for their comparison. Coloured points show seasonality values for different widths of the seasonal band between 0.2 (0.9 - 1.1) and 0.5 (0.75 - 1.25). Black points show the median over all values. Both samples show overall enhanced seasonality in the Miocene compared with the modern day.

Numerous studies have suggested the Miocene was a time of enhanced seasonality in the mid latitudes with warm-wet, cold-dry seasonal cycles in central Europe (Bruch et al., 2011; Harzhauser et al., 2011). At high latitudes, the picture is less conclusive. Pollen reconstructions from eastern Siberia suggest the Late Miocene marks the onset of modern atmospheric circulation patterns and the establishment of today's wet summer/dry winter regime, albeit with considerably higher total precipitation between 700 mm and 900 mm per year (Popova et al., 2012). At Temmirdekh-khaj and Omoloy, Miocene pollen reconstructions suggest the mean annual range in precipitation (the difference between wet and dry season amplitude) was 70

- 80 mm and 110 - 130 mm respectively. This seems large compared with today's mean summer precipitation of 169 mm and annual precipitation of 309 mm but should be viewed in context of a wetter Tortonian regime given higher moisture availability from a summer ice-free Arctic (Stein et al., 2016). Analysis of fossil wood $\delta^{13}\text{C}$ from Cherskiy (N67.7°, E161.6°) in northeastern Siberia shows a high variability in precipitation, with the wet season alternating between summer and winter (Schubert et al., 2017). In contrast, our Taba Ba'astakh records suggest an enhanced seasonal precipitation regime compared with the modern day. We propose this likely arose from differing moisture availability from the nearby Arctic Ocean which was largely sea-ice covered during the Tortonian winter and ice-free during Tortonian summers (Stein et al., 2016). This would have led to enhanced evaporation and moisture transport into northern Siberia in the summer, compared with winter. This effect appears to outweigh any impact of reduced continentality given global average sea levels ca. 10 m higher during the Late Miocene compared with modern (Miller et al., 2005). A likely return to similar ice coverage over the coming century (Sigmond et al., 2018) may drive a shift to more enhanced seasonal precipitation regimes similar to those we infer for the Tortonian.

6 Conclusions

We present the first speleothem derived temperature and precipitation seasonality records from Arctic Siberia during the Tortonian (11.63 – 7.246 Ma). Our findings offer insight into high latitude climate during a period when the global mean surface temperature was similar to that projected over the coming decades under high emission scenarios.

Apparent hydrologically driven element cycles suggest a more seasonal precipitation regime compared with the modern day, likely driven by fluctuations in Arctic Sea ice extent. Given probable reductions in summer Arctic ice extent over the coming decades, a return to more volatile precipitation regimes seems likely, with increased summer precipitation driving permafrost thaw and impacting local infrastructure.

We use two independent methodologies to reconstruct the most northerly terrestrial Tortonian temperatures between 6.6°C and 11.1°C from high latitude central Siberia. These findings provide much needed estimates for future Arctic amplification, implying Arctic MAAT increases of 18.9–23.4°C above modern, given global mean temperature rises of ca. 4.5°C above pre-industrial. This is in good agreement with previous estimates from the region. and support the consensus of a substantially warmer Late Miocene climate compared with modern day. Our findings confirm the long-established discrepancy between model simulations and proxy reconstructions, producing considerably higher estimates for Tortonian Arctic amplification than models.

Author contributions

SU and SB conceptualised the study. AV, OS, AK, IA, and SB were responsible for sample collection. AV and GH provided U-Pb dating of samples. SU and SM performed clumped isotope analysis. FL and SU milled samples and performed stable isotope analysis. PS performed trace element analysis. YD performed fluid inclusion measurements. TB and AG contributed to interpretation of the dataset, with TB providing the comparison between Miocene and modern seasonal cycles (and production of figures 6, S8 and S9). SU oversaw writing of the manuscript and figure preparation, with significant input from FL, TO, SB, and AG. All authors contributed to the review and editing of the manuscript.

Competing Interests

The authors declare that they have no conflict of interest.

580 Data availability statement

All data will be included in this manuscript in the supporting information. Trace element, stable, and clumped isotope data is archived in the Zenodo database(DOI [10.5281/zenodo.11476112](https://doi.org/10.5281/zenodo.11476112)).

Disclaimer

Any use of trade, firm, or product names is for descriptive purposes only and does not imply endorsement by the U.S.
585 Government.

Acknowledgements

The authors would like to thank the Leverhulme Trust (RPG-2020-334), Natural Environment Research Council (NE/KE005057/1 awarded to A. Vaks), and Swiss National Science Foundation (grant P2EZP2_172213 awarded to F. Lechleitner) who funded this research. We thank Julian Murton at the University of Sussex, Arthur Oldeman at Utrecht
590 University, and an anonymous reviewer for their constructive reviews and helpful comments, alongside Paul Dennis and Norbert Marwan for acting as independent reviewers of the draft manuscript, and Alberto Reyes for his role as journal editor. We thank Birgit Schröder at GFZ Potsdam for providing the Plessen internal standard used in our stable isotope measurements. TB acknowledges fruitful discussions with Norbert Marwan.

- Anderson, N. T., Kelson, J. R., Kele, S., Daëron, M., Bonifacie, M., Horita, J., Mackey, T. J., John, C. M., Kluge, T., Petschnig, P., Jost, A. B., Huntington, K. W., Bernasconi, S. M., and Bergmann, K. D.: A Unified Clumped Isotope Thermometer Calibration (0.5–1,100°C) Using Carbonate-Based Standardization, *Geophys Res Lett*, 48, <https://doi.org/10.1029/2020GL092069>, 2021.
- 600 Baker, A., Hartmann, A., Duan, W., Hankin, S., Comas-Bru, L., Cuthbert, M. O., Treble, P. C., Banner, J., Genty, D., Baldini, L. M., Bartolomé, M., Moreno, A., Pérez-Mejías, C., and Werner, M.: Global analysis reveals climatic controls on the oxygen isotope composition of cave drip water, *Nat Commun*, 10, <https://doi.org/10.1038/s41467-019-11027-w>, 2019.
- Baker, J. L., Lachniet, M. S., Chervyatsova, O., Asmerom, Y., and Polyak, V. J.: Holocene warming in western continental Eurasia driven by glacial retreat and greenhouse forcing, *Nat Geosci*, 10, 430–435, <https://doi.org/10.1038/ngeo2953>, 2017.
- 605 Bernasconi, S. M., Müller, I. A., Bergmann, K. D., and Breitenbach, S. F. M.: Reducing Uncertainties in Carbonate Clumped Isotope Analysis Through Consistent Carbonate-Based Standardization Geochemistry, *Geophysics, Geosystems*, 2895–2914, <https://doi.org/10.1029/2017GC007385>, 2018.
- Bernasconi, S. M., Daëron, M., Bergmann, K. D., Bonifacie, M., Meckler, A. N., Affek, H. P., Anderson, N., Bajnai, D., Barkan, E., Beverly, E., Blamart, D., Burgener, L., Calmels, D., Chaduteau, C., Clog, M., Davidheiser-Kroll, B., Davies, A.,
- 610 Dux, F., Eiler, J., Elliott, B., Fetrow, A. C., Fiebig, J., Goldberg, S., Hermoso, M., Huntington, K. W., Hyland, E., Ingalls, M., Jaggi, M., John, C. M., Jost, A. B., Katz, S., Kelson, J., Kluge, T., Kocken, I. J., Laskar, A., Leutert, T. J., Liang, D., Lucarelli, J., Mackey, T. J., Mangerot, X., Meinicke, N., Modestou, S. E., Müller, I. A., Murray, S., Neary, A., Packard, N., Passey, B. H., Pelletier, E., Petersen, S., Piasecki, A., Schauer, A., Snell, K. E., Swart, P. K., Tripathi, A., Upadhyay, D., Vennemann, T., Winkelstern, I., Yarian, D., Yoshida, N., Zhang, N., and Ziegler, M.: InterCarb: A Community Effort to Improve
- 615 Interlaboratory Standardization of the Carbonate Clumped Isotope Thermometer Using Carbonate Standards, *Geochemistry, Geophysics, Geosystems*, 22, <https://doi.org/10.1029/2020GC009588>, 2021.
- Berndt, D. J. and Clifford, J.: Using dynamic time warping to find patterns in time series, *Proceedings of the 3rd international conference on knowledge discovery and data mining*, 359–370, 1994.
- Boike, J., Kattenstroth, B., Abramova, K., Bornemann, N., Chetverova, A., Fedorova, I., Fröb, K., Grigoriev, M., Grüber, M.,
- 620 Kutzbach, L., Langer, M., Minke, M., Muster, S., Piel, K., Pfeiffer, E. M., Stoof, G., Westermann, S., Wischniewski, K., Wille, C., and Hubberten, H. W.: Baseline characteristics of climate, permafrost and land cover from a new permafrost observatory in the Lena River Delta, Siberia (1998–2011), *Biogeosciences*, 10, 2105–2128, <https://doi.org/10.5194/bg-10-2105-2013>, 2013.
- Boike, J., Nitzbon, J., Anders, K., Grigoriev, M., Bolshiyarov, D., Langer, M., Lange, S., Bornemann, N., Morgenstern, A.,
- 625 Schreiber, P., Wille, C., Chadburn, S., Gouttevin, I., Burke, E., and Kutzbach, L.: A 16-year record (2002–2017) of permafrost, active-layer, and meteorological conditions at the Samoylov Island Arctic permafrost research site, Lena River delta, northern

- Siberia: An opportunity to validate remote-sensing data and land surface, snow, and permafrost models, *Earth Syst Sci Data*, 11, 261–299, <https://doi.org/10.5194/essd-11-261-2019>, 2019.
- Bonne, J. L., Meyer, H., Behrens, M., Boike, J., Kipfstuhl, S., Rabe, B., Schmidt, T., Schönicke, L., Steen-Larsen, H. C., and
630 Werner, M.: Moisture origin as a driver of temporal variabilities of the water vapour isotopic composition in the Lena River
Delta, Siberia, *Atmos Chem Phys*, 20, 10493–10511, <https://doi.org/10.5194/acp-20-10493-2020>, 2020.
- Borsato, A., Frisia, S., Fairchild, I. J., Somogyi, A., and Susini, J.: Trace element distribution in annual stalagmite laminae
mapped by micrometer-resolution X-ray fluorescence: Implications for incorporation of environmentally significant species,
Geochim Cosmochim Acta, 71, 1494–1512, <https://doi.org/10.1016/j.gca.2006.12.016>, 2007.
- 635 Bradshaw, C. D., Lunt, D. J., Flecker, R., Salzmann, U., Pound, M. J., Haywood, A. M., and Eronen, J. T.: The relative roles
of CO₂ and palaeogeography in determining late Miocene climate: Results from a terrestrial model-data comparison, *Climate
of the Past*, 8, 1257–1285, <https://doi.org/10.5194/cp-8-1257-2012>, 2012.
- Brand, W. A., Assonov, S. S., and Coplen, T. B.: Correction for the ¹⁷O interference in $\delta(^{13}\text{C})$ measurements when analyzing
CO₂ with stable isotope mass spectrometry (IUPAC Technical Report), *Pure and Applied Chemistry*, 82, 1719–1733,
640 <https://doi.org/10.1351/PAC-REP-09-01-05>, 2010.
- Breitenbach, S. F. M. and Marwan, N.: Acquisition and analysis of greyscale data from stalagmites using ImageJ software,
69–78 pp., 2023.
- Bruch, A. A., Utescher, T., and Mosbrugger, V.: Precipitation patterns in the Miocene of Central Europe and the development
of continentality, *Palaeogeogr Palaeoclimatol Palaeoecol*, 304, 202–211, <https://doi.org/10.1016/j.palaeo.2010.10.002>, 2011.
- 645 Buchwal, A., Rachlewicz, G., Heim, B., and Juhls, B.: Trees on the tundra: warmer climate might not favor prostrate Larix
tree but Betula nana shrub growth in Siberian tundra (Lena River Delta), *Agric For Meteorol*, 339,
<https://doi.org/10.1016/j.agrformet.2023.109543>, 2023.
- Burls, N. J., Bradshaw, C. D., De Boer, A. M., Herold, N., Huber, M., Pound, M., Donnadieu, Y., Farnsworth, A., Frigola, A.,
Gasson, E., von der Heydt, A. S., Hutchinson, D. K., Knorr, G., Lawrence, K. T., Lear, C. H., Li, X., Lohmann, G., Lunt, D.
650 J., Marzocchi, A., Prange, M., Riihimäki, C. A., Sarr, A. C., Siler, N., and Zhang, Z.: Simulating Miocene Warmth: Insights
From an Opportunistic Multi-Model Ensemble (MioMIP1), *Paleoceanogr Paleoclimatol*, 36,
<https://doi.org/10.1029/2020PA004054>, 2021.
- Chylek, P., Folland, C., Klett, J. D., Wang, M., Hengartner, N., Lesins, G., and Dubey, M. K.: Annual Mean Arctic
Amplification 1970–2020: Observed and Simulated by CMIP6 Climate Models, *Geophys Res Lett*, 49,
655 <https://doi.org/10.1029/2022GL099371>, 2022.
- Coplen, T. B.: Calibration of the calcite–water oxygen-isotope geothermometer at Devils Hole, Nevada, a natural laboratory,
Geochim Cosmochim Acta, 71, 3948–3957, <https://doi.org/10.1016/j.gca.2007.05.028>, 2007.
- Craig, H.: Isotopic variations in meteoric waters, *Science* (1979), 133, 1702–1703,
<https://doi.org/10.1126/science.133.3465.1702>, 1961.

- 660 Daëron, M.: Full Propagation of Analytical Uncertainties in $\Delta 47$ Measurements, *Geochemistry, Geophysics, Geosystems*, 22, <https://doi.org/10.1029/2020GC009592>, 2021.
- Daëron, M. and Gray, W. R.: Revisiting Oxygen-18 and Clumped Isotopes in Planktic and Benthic Foraminifera, *Paleoceanogr Paleoclimatol*, 38, <https://doi.org/10.1029/2023PA004660>, 2023.
- Daëron, M., Blamart, D., Peral, M., and Affek, H. P.: Absolute isotopic abundance ratios and the accuracy of $\Delta 47$ measurements, *Chem Geol*, 442, 83–96, <https://doi.org/10.1016/j.chemgeo.2016.08.014>, 2016.
- 665 Dansgaard, W.: Stable isotopes in precipitation, *Tellus*, 16, 436–468, <https://doi.org/10.3402/tellusa.v16i4.8993>, 1964.
- Dennis, K. J., Affek, H. P., Passey, B. H., Schrag, D. P., and Eiler, J. M.: Defining an absolute reference frame for ‘clumped’ isotope studies of CO_2 , *Geochim Cosmochim Acta*, 75, 7117–7131, <https://doi.org/10.1016/j.gca.2011.09.025>, 2011.
- Domínguez-Villar, D., Fairchild, I. J., Baker, A., Carrasco, R. M., and Pedraza, J.: Reconstruction of cave air temperature based on surface atmosphere temperature and vegetation changes: Implications for speleothem palaeoclimate records, *Earth Planet Sci Lett*, 369–370, 158–168, <https://doi.org/10.1016/j.epsl.2013.03.017>, 2013.
- 670 Dublyansky, Y. V. and Spötl, C.: Hydrogen and oxygen isotopes of water from inclusions in minerals: Design of a new crushing system and on-line continuous-flow isotope ratio mass spectrometric analysis, *Rapid Communications in Mass Spectrometry*, 23, 2605–2613, <https://doi.org/10.1002/rcm.4155>, 2009.
- 675 Eiler, J. M. and Schauble, E.: $18\text{O}13\text{C}16\text{O}$ in Earth’s atmosphere, *Geochim Cosmochim Acta*, 68, 4767–4777, <https://doi.org/10.1016/j.gca.2004.05.035>, 2004.
- Fernandez, A., Müller, I. A., Rodríguez-Sanz, L., van Dijk, J., Looser, N., and Bernasconi, S. M.: A Reassessment of the Precision of Carbonate Clumped Isotope Measurements: Implications for Calibrations and Paleoclimate Reconstructions, *Geochemistry, Geophysics, Geosystems*, 18, 4375–4386, <https://doi.org/10.1002/2017GC007106>, 2017.
- 680 Finestone, E. M., Breeze, P. S., Breitenbach, S. F. M., Drake, N., Bergmann, L., Maksudov, F., Muhammadiyev, A., Scott, P., Cai, Y., Khatsenovich, A. M., Rybin, E. P., Nehrke, G., Boivin, N., and Petraglia, M.: Paleolithic occupation of arid Central Asia in the Middle Pleistocene, *PLoS One*, 17, <https://doi.org/10.1371/journal.pone.0273984>, 2022.
- Ford, J. D., McDowell, G., and Pearce, T.: The adaptation challenge in the Arctic, <https://doi.org/10.1038/nclimate2723>, 1 December 2015.
- 685 Gaskell, D. E., Huber, M., O’Brien, C. L., Inglis, G. N., Acosta, R. P., Poulsen, C. J., and Hull, P. M.: The latitudinal temperature gradient and its climate dependence as inferred from foraminiferal $\delta 18\text{O}$ over the past 95 million years, 119, 2111332119, <https://doi.org/10.1073/pnas>, 2022.
- Goldner, A., Herold, N., and Huber, M.: The challenge of simulating the warmth of the mid-Miocene climatic optimum in CESM1, *Climate of the Past*, 10, 523–536, <https://doi.org/10.5194/cp-10-523-2014>, 2014.
- 690 Hamma, J.: Drivers of permafrost degradation along the Inuvik to Tuktoyaktuk Highway (ITH), University of Potsdam, 2022.
- Hartland, A., Fairchild, I. J., Lead, J. R., Borsato, A., Baker, A., Frisia, S., and Baalousha, M.: From soil to cave: Transport of trace metals by natural organic matter in karst dripwaters, *Chem Geol*, 304–305, 68–82, <https://doi.org/10.1016/j.chemgeo.2012.01.032>, 2012.

- Harzhauser, M., Piller, W. E., Müllegger, S., Grunert, P., and Micheels, A.: Changing seasonality patterns in Central Europe
695 from Miocene Climate Optimum to Miocene Climate Transition deduced from the *Crassostrea* isotope archive, *Glob Planet Change*, 76, 77–84, <https://doi.org/10.1016/j.gloplacha.2010.12.003>, 2011.
- Hao, Q., Wang, L., Oldfield, F., and Guo, Z.: Extra-long interglacial in Northern Hemisphere during MISs 15-13 arising from limited extent of Arctic ice sheets in glacial MIS 14, *Sci Rep*, 5, <https://doi.org/10.1038/srep12103>, 2015.
- Herbert, T. D., Lawrence, K. T., Tzanova, A., Peterson, L. C., Caballero-Gill, R., and Kelly, C. S.: Late Miocene global cooling
700 and the rise of modern ecosystems, *Nat Geosci*, 9, 843–847, <https://doi.org/10.1038/ngeo2813>, 2016.
- Hofer, S., Lang, C., Amory, C., Kittel, C., Delhasse, A., Tedstone, A., and Fettweis, X.: Greater Greenland Ice Sheet contribution to global sea level rise in CMIP6, *Nat Commun*, 11, <https://doi.org/10.1038/s41467-020-20011-8>, 2020.
- Huntington, K. W., Eiler, J. M., Affek, H. P., Guo, W., Bonifacie, M., Yeung, L. Y., Thiagarajan, N., Passey, B., Tripathi, A., Daëron, M., and Came, R.: Methods and limitations of “clumped” CO₂ isotope ($\Delta 47$) analysis by gas-source isotope ratiomass
705 spectrometry, *Journal of Mass Spectrometry*, 44, 1318–1329, <https://doi.org/10.1002/jms.1614>, 2009.
- Izokh, N. and Yazikov, A.: Discovery of Early Carboniferous conodonts in Northern Kharaulakh Ranges (lower reaches of the Lena River, northeastern Siberia, Arctic Russia), *Revue de Micropaleontologie*, 60, 213–232, <https://doi.org/10.1016/j.revmic.2017.03.001>, 2017.
- Strauss, J., Fuchs, M., Hugelius, G., Miesner, F., Nitze, I., Opfergelt, S., Schuur, E., Treat, C., Turetsky, M., Yang, Y., and
710 Grosse, G.: Organic matter storage and vulnerability in the permafrost domain, in: Reference Module in Earth Systems and Environmental Sciences, Elsevier, <https://doi.org/https://doi.org/10.1016/B978-0-323-99931-1.00164-1>, 2024.
- John, C. M. and Bowen, D.: Community software for challenging isotope analysis: First applications of ‘Easotope’ to clumped isotopes, *Rapid Communications in Mass Spectrometry*, 30, 2285–2300, <https://doi.org/10.1002/rcm.7720>, 2016.
- Johnson, K. R., Hu, C., Belshaw, N. S., and Henderson, G. M.: Seasonal trace-element and stable-isotope variations in a
715 Chinese speleothem: The potential for high-resolution paleomonsoon reconstruction, *Earth Planet Sci Lett*, 244, 394–407, <https://doi.org/10.1016/j.epsl.2006.01.064>, 2006.
- Lachniet, M. S.: Climatic and environmental controls on speleothem oxygen-isotope values, *Quat Sci Rev*, 28, 412–432, <https://doi.org/10.1016/j.quascirev.2008.10.021>, 2009.
- Lechleitner, F. A., Mason, A. J., Breitenbach, S. F. M., Vaks, A., Haghipour, N., and Henderson, G. M.: Permafrost-related
720 hiatuses in stalagmites: Evaluating the potential for reconstruction of carbon cycle dynamics, *Quat Geochronol*, 56, <https://doi.org/10.1016/j.quageo.2019.101037>, 2020.
- Ma, N., Jiang, J. H., Hou, K., Lin, Y., Vu, T., Rosen, P. E., Gu, Y., and Fahy, K. A.: 21st Century Global and Regional Surface Temperature Projections, *Earth and Space Science*, 9, <https://doi.org/10.1029/2022EA002662>, 2022.
- Mason, A. J., Vaks, A., Breitenbach, S. F. M., Hooker, J. N., and Henderson, G. M.: A simplified isotope dilution approach
725 for the U-Pb dating of speleogenic and other low-²³²Th carbonates by multi-collector ICP-MS, *Geochronology*, 4, 33–54, <https://doi.org/10.5194/gchron-4-33-2022>, 2022.

- Masson-Delmotte, Valerie, Zhai, P., Pirani, A., Connors, S. L., Pean, C., Berger, S., Caud, N., Chen, Y., Goldfarb, L., Gomis, M., and others: Climate change 2021: the physical science basis, Contribution of working group I to the sixth assessment report of the intergovernmental panel on climate change, 2, 2021.
- 730 McKay, D. I. A., Staal, A., Abrams, J. F., Winkelmann, R., Sakschewski, B., Loriani, S., Fetzer, I., Cornell, S. E., Rockström, J., and Lenton, T. M.: Exceeding 1.5°C global warming could trigger multiple climate tipping points, *Science* (1979), 377, <https://doi.org/10.1126/science.abn7950>, 2022.
- Meinicke, N., Ho, S. L., Hannisdal, B., Nürnberg, D., Tripathi, A., Schiebel, R., and Meckler, A. N.: A robust calibration of the clumped isotopes to temperature relationship for foraminifers, *Geochim Cosmochim Acta*, 270, 160–183, <https://doi.org/10.1016/j.gca.2019.11.022>, 2020.
- 735 Met Office Heathrow climatic averages 1991 – 2000, Retrieved 22 October 2024. Available at: <https://www.metoffice.gov.uk/research/climate/maps-and-data/uk-climate-averages/gcpsvg3nc>
- Micheels, A., Bruch, A. A., Uhl, D., Utescher, T., and Mosbrugger, V.: A Late Miocene climate model simulation with ECHAM4/ML and its quantitative validation with terrestrial proxy data, *Palaeogeogr Palaeoclimatol Palaeoecol*, 253, 251–
- 740 270, <https://doi.org/10.1016/j.palaeo.2007.03.042>, 2007.
- Mikhailov et al.: Russian-German Cooperation: Expeditions to Siberia in 2017, edited by: Jens Strauss, Alfred-Wegener Institute, 90–107, 2018.
- Miller, K. G., Kominz, M. A., Browning, J. V., Wright, J. D., Mountain, G. S., Katz, M. E., Sugarman, P. J., Cramer, B. S., Christie-Blick, N., and Pekar, S. F.: The Phanerozoic Record of Global Sea-Level Change, *Science* (1979), 310, 1293–1298,
- 745 2005.
- Miller, K. G., Browning, J. V., Schmelz, W. J., Kopp, R. E., Mountain, G. S., and Wright, J. D.: Cenozoic sea-level and cryospheric evolution from deep-sea geochemical and continental margin records, 2020.
- Milne, C. J., Kinniburgh, D. G., Van Riemsdijk, W. H., and Tipping, E.: Generic NICA - Donnan model parameters for metal-ion binding by humic substances, *Environ Sci Technol*, 37, 958–971, <https://doi.org/10.1021/es0258879>, 2003.
- 750 Moberg, A. Stockholm Historical Weather Observations — Monthly mean air temperatures since 1756. Dataset version 3. Bolin Centre Database. <https://doi.org/10.17043/stockholm-historical-monthly-temperature-3>, 2021.
- Molnar, P.: Differences between soil and air temperatures: Implications for geological reconstructions of past climate, *Geosphere*, 18, 800–824, <https://doi.org/10.1130/GES02448.1>, 2022.
- Moseley, G. E., Edwards, R. L., Lord, N. S., Spötl, C., and Cheng, H.: Speleothem record of mild and wet mid-Pleistocene climate in northeast Greenland, *Sci. Adv.*, 2021.
- 755 Nazarenko, L. S., Tausnev, N., Russell, G. L., Rind, D., Miller, R. L., Schmidt, G. A., Bauer, S. E., Kelley, M., Ruedy, R., Ackerman, A. S., Aleinov, I., Bauer, M., Bleck, R., Canuto, V., Cesana, G., Cheng, Y., Clune, T. L., Cook, B. I., Cruz, C. A., Del Genio, A. D., Elsaesser, G. S., Faluvegi, G., Kiang, N. Y., Kim, D., Lacis, A. A., Leboissetier, A., LeGrande, A. N., Lo, K. K., Marshall, J., Matthews, E. E., McDermid, S., Mezuman, K., Murray, L. T., Oinas, V., Orbe, C., García-Pando, C. P., Perlwitz, J. P., Puma, M. J., Romanou, A., Shindell, D. T., Sun, S., Tsigaridis, K.,

- 760 Tselioudis, G., Weng, E., Wu, J., and Yao, M. S.: Future Climate Change Under SSP Emission Scenarios With GISS-E2.1, *J Adv Model Earth Syst*, 14, <https://doi.org/10.1029/2021MS002871>, 2022.
- Nitzbon, J., Schneider von Deimling, T., Aliyeva, M., Chadburn, S. E., Grosse, G., Laboor, S., Lee, H., Lohmann, G., Steinert, N. J., Stuenzi, S. M., Werner, M., Westermann, S., & Langer, M. No respite from permafrost-thaw impacts in the absence of a global tipping point. *Nature Climate Change*, 14(6), 573–585. <https://doi.org/10.1038/s41558-024-02011-4>. 2024
- 765 de Nooijer, W., Zhang, Q., Li, Q., Zhang, Q., Li, X., Zhang, Z., Guo, C., Nisancioglu, K. H., Haywood, A. M., Tindall, J. C., Hunter, S. J., Dowsett, H. J., Stepanek, C., Lohmann, G., Otto-Bliesner, B. L., Feng, R., Sohl, L. E., Chandler, M. A., Tan, N., Contoux, C., Ramstein, G., Baatsen, M. L. J., Von Der Heydt, A. S., Chandan, D., Peltier, W. R., Abe-Ouchi, A., Chan, W. Le, Kamae, Y., and Brierley, C. M.: Evaluation of Arctic warming in mid-Pliocene climate simulations, *Climate of the Past*, 16, 2325–2341, <https://doi.org/10.5194/cp-16-2325-2020>, 2020.
- 770 Opel, T., Bertran, P., Grosse, G., Jones, M., Luetscher, M., Schirrmeister, L., Stadelmaier, K. H., and Veremeeva, A.: Ancient permafrost and past permafrost in the Northern Hemisphere. In: Elias, S. (eds.) *Encyclopedia of Quaternary Science*, 3rd Edition. vol. 5, pp. 16-33. UK: Elsevier. [dx.doi.org/10.1016/B978-0-323-99931-1.00258-0](https://doi.org/10.1016/B978-0-323-99931-1.00258-0), 2025.
- Orland, I. J., Burstyn, Y., Bar-Matthews, M., Kozdon, R., Ayalon, A., Matthews, A., and Valley, J. W.: Seasonal climate signals (1990–2008) in a modern Soreq Cave stalagmite as revealed by high-resolution geochemical analysis, *Chem Geol*, 363, 322–333, <https://doi.org/10.1016/j.chemgeo.2013.11.011>, 2014.
- 775 Oster, J. L., Ronay, E. R., Sharp, W. D., Breitenbach, S. F. M., and Furbish, D. J.: Controls on Speleothem Initial $^{234}\text{U}/^{238}\text{U}$ Ratios in a Monsoon Climate, *Geochemistry, Geophysics, Geosystems*, 24, <https://doi.org/10.1029/2023GC010899>, 2023.
- Peel, M. C., Finlayson, B. L., and McMahon, T. A.: Hydrology and Earth System Sciences Updated world map of the Köppen-Geiger climate classification, *Hydrol. Earth Syst. Sci*, 1633–1644 pp., 2007.
- 780 Petersen, S. V., Winkelstern, I. Z., Lohmann, K. C., and Meyer, K. W.: The effects of Porapak(TM) trap temperature on $\delta^{18}\text{O}$, $\delta^{13}\text{C}$, and D_47 values in preparing samples for clumped isotope analysis, *Rapid Communications in Mass Spectrometry*, 30, 1–10, <https://doi.org/10.1002/rcm.7438>, 2015.
- Pflitsch, A. and Piasecki, J.: Detection of an airflow system in Niedzwiedzia (Bear) Cave, Kletno, Poland, *Journal of Cave and Karst Studies*, 65, 160–173, 2003.
- 785 Pionke, H. B., Gburek, W. J., Sharpley, A. N., and Zollweg, J. A.: Hydrological and chemical controls on phosphorus loss from catchments, in: *Phosphorus Loss From Soil to Water*, CAB International, Wallingford, 225–242, 1997.
- Popova, S., Utescher, T., Gromyko, D., Bruch, A. A., and Mosbrugger, V.: Palaeoclimate evolution in Siberia and the Russian far east from the Oligocene to Pliocene - evidence from fruit and seed floras, *Turkish Journal of Earth Sciences*, 21, 315–334, <https://doi.org/10.3906/yer-1005-6>, 2012.
- 790 Pound, M. J., Haywood, A. M., Salzmann, U., Riding, J. B., Lunt, D. J., and Hunter, S. J.: A Tortonian (Late Miocene, 11.61–7.25Ma) global vegetation reconstruction, *Palaeogeogr Palaeoclimatol Palaeoecol*, 300, 29–45, <https://doi.org/10.1016/j.palaeo.2010.11.029>, 2011.

- Pound, M. J., Haywood, A. M., Salzmann, U., and Riding, J. B.: Global vegetation dynamics and latitudinal temperature gradients during the Mid to Late Miocene (15.97–5.33Ma), <https://doi.org/10.1016/j.earscirev.2012.02.005>, April 2012.
- 795 Rae, J. W. B., Zhang, Y. G., Liu, X., Foster, G. L., Stoll, H. M., and Whiteford, R. D. M.: Atmospheric CO₂ over the Past 66 Million Years from Marine Archives, *The Annual Review of Earth and Planetary Sciences* is online at earth.annualreviews.org, 49, 609–650, <https://doi.org/10.1146/annurev-earth-082420>, 2021.
- Rantanen, M., Karpechko, A. Y., Lipponen, A., Nordling, K., Hyvärinen, O., Ruosteenoja, K., Vihma, T., and Laaksonen, A.: The Arctic has warmed nearly four times faster than the globe since 1979, *Commun Earth Environ*, 3,
800 <https://doi.org/10.1038/s43247-022-00498-3>, 2022.
- Rodrigues, T., Voelker, A. H. L., Grimalt, J. O., Abrantes, F., and Naughton, F.: Iberian Margin sea surface temperature during MIS 15 to 9 (580–300 ka): Glacial suborbital variability versus interglacial stability, *Paleoceanography*, 26, <https://doi.org/10.1029/2010PA001927>, 2011.
- Schubert, B. A., Jahren, A. H., Davydov, S. P., and Warny, S.: The transitional climate of the late Miocene Arctic: Winter
805 dominated precipitation with high seasonal variability, *Geology*, 45, 447–450, <https://doi.org/10.1130/G38746.1>, 2017.
- Sherwin, C. M. and Baldini, J. U. L.: Cave air and hydrological controls on prior calcite precipitation and stalagmite growth rates: Implications for palaeoclimate reconstructions using speleothems, *Geochim Cosmochim Acta*, 75, 3915–3929, <https://doi.org/10.1016/j.gca.2011.04.020>, 2011.
- Sigmond, M., Fyfe, J. C., and Swart, N. C.: Ice-free Arctic projections under the Paris Agreement, *Nat Clim Chang*, 8, 404–
810 408, <https://doi.org/10.1038/s41558-018-0124-y>, 2018.
- Sliwinski, J. T., Kost, O., Endres, L., Iglesias, M., Haghipour, N., González-Lemos, S., and Stoll, H. M.: Exploring soluble and colloidally transported trace elements in stalagmites: The strontium-yttrium connection, *Geochim Cosmochim Acta*, 343, 64–83, <https://doi.org/10.1016/j.gca.2022.12.023>, 2023.
- Smith, D. M., Scaife, A. A., Eade, R., Athanasiadis, P., Bellucci, A., Bethke, I., Bilbao, R., Borchert, L. F., Caron, L. P.,
815 Counillon, F., Danabasoglu, G., Delworth, T., Doblas-Reyes, F. J., Dunstone, N. J., Estella-Perez, V., Flavoni, S., Hermanson, L., Keenlyside, N., Kharin, V., Kimoto, M., Merryfield, W. J., Mignot, J., Mochizuki, T., Modali, K., Monerie, P. A., Müller, W. A., Nicolí, D., Ortega, P., Pankatz, K., Pohlmann, H., Robson, J., Ruggieri, P., Sospedra-Alfonso, R., Swingedouw, D., Wang, Y., Wild, S., Yeager, S., Yang, X., and Zhang, L.: North Atlantic climate far more predictable than models imply, *Nature*, 583, 796–800, <https://doi.org/10.1038/s41586-020-2525-0>, 2020.
- 820 Sosdian, S. M., Greenop, R., Hain, M. P., Foster, G. L., Pearson, P. N., and Lear, C. H.: Constraining the evolution of Neogene ocean carbonate chemistry using the boron isotope pH proxy, *Earth Planet Sci Lett*, 498, 362–376, <https://doi.org/10.1016/j.epsl.2018.06.017>, 2018.
- Spors, S.: Stable Water Isotope Characteristics of Recent Precipitation from Tiksi and Samoylov Island-Calibration of a Geoscientific Proxy for Northern Siberia: Bachelors Thesis, Institut für Erd- und Umweltwissenschaften, Universität Potsdam,
825 Potsdam, 2018.

- Spótl, C. and Vennemann, T. W.: Continuous-flow isotope ratio mass spectrometric analysis of carbonate minerals, <https://doi.org/10.1002/rcm.1010>, 2003.
- Stein, R., Fahl, K., Schreck, M., Knorr, G., Niessen, F., Forwick, M., Gebhardt, C., Jensen, L., Kaminski, M., Kopf, A., Matthiessen, J., Jokat, W., and Lohmann, G.: Evidence for ice-free summers in the late Miocene central Arctic Ocean, *Nat Commun*, 7, <https://doi.org/10.1038/ncomms11148>, 2016.
- Steinthorsdottir, M., Jardine, P. E., and Rember, W. C.: Near-Future $p\text{CO}_2$ During the Hot Miocene Climatic Optimum, *Paleoceanogr Paleoclimatol*, 36, <https://doi.org/10.1029/2020PA003900>, 2021a.
- Steinthorsdottir, M., Coxall, H. K., de Boer, A. M., Huber, M., Barbolini, N., Bradshaw, C. D., Burls, N. J., Feakins, S. J., Gasson, E., Henderiks, J., Holbourn, A. E., Kiel, S., Kohn, M. J., Knorr, G., Kürschner, W. M., Lear, C. H., Liebrand, D., Lunt, D. J., Mörs, T., Pearson, P. N., Pound, M. J., Stoll, H., and Strömberg, C. A. E.: The Miocene: The Future of the Past, *Paleoceanogr Paleoclimatol*, 36, <https://doi.org/10.1029/2020PA004037>, 2021b.
- Stoll, H. M., Müller, W., and Prieto, M.: I-STAL, a model for interpretation of Mg/Ca, Sr/Ca and Ba/Ca variations in speleothems and its forward and inverse application on seasonal to millennial scales, *Geochemistry, Geophysics, Geosystems*, 13, <https://doi.org/10.1029/2012GC004183>, 2012.
- Super, J. R., Thomas, E., Pagani, M., Huber, M., O'Brien, C., and Hull, P. M.: North Atlantic temperature and $p\text{CO}_2$ coupling in the early-middle Miocene, *Geology*, 46, 519–522, <https://doi.org/10.1130/G40228.1>, 2018.
- Taylor, P. C., Boeke, R. C., Boisvert, L. N., Feldl, N., Henry, M., Huang, Y., Langen, P. L., Liu, W., Pithan, F., Sejas, S. A., and Tan, I.: Process Drivers, Inter-Model Spread, and the Path Forward: A Review of Amplified Arctic Warming, <https://doi.org/10.3389/feart.2021.758361>, 9 February 2022.
- Töchterle, P., Baldo, A., Murton, J. B., Schenk, F., Lawrence Edwards, R., Koltai, G., and Moseley, G. E.: Reconstructing Younger Dryas ground temperature and snow thickness from cave deposits, *Climate of the Past*, 20, 1521–1535, <https://doi.org/10.5194/cp-20-1521-2024>, 2024.
- Tooth, A. F. and Fairchild, I. J.: Soil and karst aquifer hydrological controls on the geochemical evolution of speleothem-forming drip waters, Crag Cave, southwest Ireland, *J Hydrol (Amst)*, 273, 2003.
- Treble, P. C., Fairchild, I. J., Griffiths, A., Baker, A., Meredith, K. T., Wood, A., and McGuire, E.: Impacts of cave air ventilation and in-cave prior calcite precipitation on Golgotha Cave dripwater chemistry, southwest Australia, *Quat Sci Rev*, 127, 61–72, <https://doi.org/10.1016/j.quascirev.2015.06.001>, 2015.
- Tremaine, D. M. and Froelich, P. N.: Speleothem trace element signatures: A hydrologic geochemical study of modern cave dripwaters and farmed calcite, *Geochim Cosmochim Acta*, 121, 522–545, <https://doi.org/10.1016/j.gca.2013.07.026>, 2013.
- Tremaine, D. M., Froelich, P. N., and Wang, Y.: Speleothem calcite farmed in situ: Modern calibration of $\delta^{18}\text{O}$ and $\delta^{13}\text{C}$ paleoclimate proxies in a continuously-monitored natural cave system, *Geochim Cosmochim Acta*, 75, 4929–4950, <https://doi.org/10.1016/j.gca.2011.06.005>, 2011.

- Vaks, A., Mason, A. J., Breitenbach, S. F. M., Kononov, A. M., Osinzev, A. V., Rosensaft, M., Borshevsky, A., Gutareva, O. S., and Henderson, G. M.: Palaeoclimate evidence of vulnerable permafrost during times of low sea ice, *Nature*, 577, 221–225, <https://doi.org/10.1038/s41586-019-1880-1>, 2020.
- Vaks, A., Mason, A., Breitenbach, S.F.M., Giesche, A., Osinzev, A., Yakshina, I., Kononov, A., Umbo, S., Lechleitner, F., Rosensaft, M. Borshevsky, A., and Henderson, G. M. Arctic speleothems reveal Late Miocene permafrost-free Northern Hemisphere, *Nature Comms.* (accepted)
- Vihma, T.: Effects of Arctic Sea Ice Decline on Weather and Climate: A Review, *Surv Geophys*, 35, 1175–1214, <https://doi.org/10.1007/s10712-014-9284-0>, 2014.
- Wassenburg, J. A., Riechelmann, S., Schröder-Ritzrau, A., Riechelmann, D. F. C., Richter, D. K., Immenhauser, A., Terente, M., Constantin, S., Hachenberg, A., Hansen, M., and Scholz, D.: Calcite Mg and Sr partition coefficients in cave environments: Implications for interpreting prior calcite precipitation in speleothems, *Geochim Cosmochim Acta*, 269, 581–596, <https://doi.org/10.1016/j.gca.2019.11.011>, 2020.
- Westerhold, T., Marwan, N., Drury, A. J., Liebrand, D., Agnini, C., Anagnostou, E., Barnet, J. S. K., Bohaty, S. M., De Vleeschouwer, D., Florindo, F., Frederichs, T., Hodell, D. A., Holbourn, A. E., Kroon, D., Lauretano, V., Littler, K., Lourens, L. J., Lyle, M., Pälike, H., Röhl, U., Tian, J., Wilkens, R. H., Wilson, P. A., and Zachos, J. C.: An astronomically dated record of Earth’s climate and its predictability over the last 66 million years, *Science* (1979), 369, 1383–1388, <https://doi.org/10.1126/SCIENCE.ABA6853>, 2020.
- Wigley, T. M. L. and Brown, M. C.: The physics of caves: in Ford, T.D. & Cullingford, C.H.D (eds.), in: *The Science of Speleology*, Academic Press, London, 329–358, 1976.
- Xie, A., Zhu, J., Kang, S., Qin, X., Xu, B., and Wang, Y.: Polar amplification comparison among Earth’s three poles under different socioeconomic scenarios from CMIP6 surface air temperature, *Sci Rep*, 12, <https://doi.org/10.1038/s41598-022-21060-3>, 2022.
- York, D., Evensen, N. M., Martínez, M. L., and De Basabe Delgado, J.: Unified equations for the slope, intercept, and standard errors of the best straight line, *Am J Phys*, 72, 367–375, <https://doi.org/10.1119/1.1632486>, 2004.